

A pressure-based high resolution numerical method for resistive MHD



Carlos M. Xisto^{*,1,2}, José C. Páscoa¹, Paulo J. Oliveira¹

Departamento de Engenharia Electromecânica, Universidade da Beira Interior, Covilhã 6201-001, Portugal

ARTICLE INFO

Article history:

Received 26 March 2014

Received in revised form 29 June 2014

Accepted 2 July 2014

Available online 15 July 2014

Keywords:

MHD

Compressible flow

PISO

AUSM

MPD

ABSTRACT

In the paper we describe in detail a numerical method for the resistive magnetohydrodynamic (MHD) equations involving viscous flow and report the results of application to a number of typical MHD test cases. The method is of the finite volume type but mixes aspects of pressure-correction and density based solvers; the algorithm arrangement is patterned on the well-known PISO algorithm, which is a pressure method, while the flux computation makes use of the AUSM-MHD scheme, which originates from density based methods. Five groups of test cases are addressed to verify and validate the method. We start with two resistive MHD cases, namely the Shercliff and Hunt flow problems, which are intended to validate the method for low-speed resistive MHD flows. The remaining three test cases, namely the cloud-shock interaction, the MHD rotor and the MHD blast wave, are standard 2D ideal MHD problems that serve to validate the method under high-speed flow and complex interaction of MHD shocks. Finally, we demonstrate the method with a more complex application problem, and discuss results of simulation for a quasi-bi-dimensional self-field magnetoplasmadynamic (MPD) thruster, for which we study the effect of cathode length upon the electromagnetic nozzle performance.

© 2014 Elsevier Inc. All rights reserved.

1. Introduction

Numerical codes are indispensable tools for the investigation of electric propulsion systems. The application of such codes in the design of magnetoplasmadynamic (MPD) thrusters is of practical importance because they allow the aeronautical engineer to understand the effects of relevant flow-field parameters which are otherwise quite hard to analyze with experiments. Such complex analysis can be readily handled with an adequate magnetohydrodynamic (MHD) solver with the possibility of capturing MHD shocks monotonically and, at the same time, being stable in the presence of strong magnetic fields [1].

Several shock-capturing methods have been developed for the prediction of ideal MHD flows and may be classified into two groups. One group of schemes incorporate the full 7-wave structure of the MHD equations [2–7], while the other replace the 7-wave analysis by an approximation which only takes into account the maximal wave speeds, e.g. [8–12]

* Corresponding author at: Departamento de Engenharia Electromecânica, Universidade da Beira Interior, Covilhã, 6201-001, Portugal.

E-mail addresses: xisto@ubi.pt (C.M. Xisto), pascoa@ubi.pt (J.C. Páscoa), pjpo@ubi.pt (P.J. Oliveira).

URL: <http://clusterdem.ubi.pt> (C.M. Xisto).

¹ C-MAST: Center for Mechanical and Aerospace Science and Technology, Research Unit No. 151.

² Supported by the Portuguese Foundation for Science and Technology (FCT) with grant Nr. SFRH/BD/60285/2009 and project Nr. PTDC/CTESPA/114163/2009.

and Balsara et al. [13–15]. Such approximation normally tends to reduce the accuracy of the MHD solver, however AMR techniques of Balsara [16] and Keppens et al. [17] can be added to the scheme in order to increase the resolution of MHD discontinuities. Those two groups of schemes were developed in the framework of density-based solvers and they are usually applied to the solution of compressible MHD equations at moderate or high Mach number flows. However, nowadays a great number of numerical gas dynamics codes are able to solve the compressible Navier–Stokes equations without MHD effects at arbitrary Mach number regimes [18–21]. Similarly a pressure-correction solver for the all-Mach number MHD equations was proposed by van der Heul et al. [22]. This method starts from a Mach number-based non-dimensional formulation of the MHD equations and [22] demonstrated that it fulfills the requirements of Mach-uniform methods. Xisto et al. [23] have also proposed a pressure-based method for the ideal MHD equations at arbitrary Mach number flows, which was designed along the PISO algorithm arrangement ideas.

An MPD thruster, in its most basic form, consists in a central cathode surrounded by a concentric anode [24]. With such coaxial geometrical shape is quite hard to apply experimental visualization techniques to analyze the plasma flow. The use of measuring probes can also be problematic since they tend to disturb the flow. To overcome such problems Toki et al. [25] developed a two-dimensional device with a multichannel configuration. With their approach an almost uniform current distribution can be obtained along the line of sight, which ensures easier optical accessibility to the discharge region. It is obvious that a 2D configuration does not faithfully represent the features of coaxial devices. Nevertheless, the easier optical accessibility makes it possible to use advanced visualization techniques in order to relate the flow data with the performance data [26]. The huge amount of data that can thus be collected, within a quasi-bi-dimensional system, is also very useful for the validation of numerical codes applied to the computation of 3D or 2D axisymmetric MPD nozzles.

Simulation of the complex physics associated with an MPD device is not a trivial task. Some of the earlier models assumed that the plasma flow in MPD nozzles behaves like a single conducting fluid [27,28]. However, this assumption leads to some ambiguity in the definition of the plasma transport coefficients, since these are usually defined differently for the electrons and the heavy species [29]. Nevertheless, a single fluid approach can still be useful for a better understanding of the main acceleration mechanisms that are generated by this kind of systems [30]. Another approach is to consider the plasma as a single fluid, but having different temperatures for the heavy species and the electrons [1,31–33]. With this last approach it is possible to compatibilize the simplicity of the single fluid approach and, at the same time, to compute the two distinct transport coefficients in a more realistic way.

In the present paper we describe a pressure-based MHD method, under a finite volume formulation, show validation results for standard MHD test case problems and present complex application results for a self-field MPD thruster. This new algorithm was developed for the single fluid resistive magnetohydrodynamic equations and is based on an all-Mach number version of PISO [21], which was previously extended and validated for ideal MHD flow gases by Xisto et al. [23]. We will show that our pressure-based method, coupled with AUSM-type fluxes originated from density-based methods, can handle a high variety of flows, ranging from the nearly incompressible to the high compressible regimes. For multi-dimensional MHD flows, in order to minimize errors associated with $\nabla \cdot \mathbf{B} \neq 0$ we have implemented the hyperbolic/parabolic divergence cleaning technique of Dedner et al. [34] denoted GLM for generalized Lagrange multipliers. Several other methods exist and in particular it is known that the constrained transport methods are more accurate and stable [35,36], since they do not suffer from non-conservative problems as may occur in the GLM formulation of [34]. However we applied here the GLM and we have observed a satisfactory behavior during the computation of the validation cases. For future, more stringent problems, other methods may be envisaged, such as those of [35].

In the next section we state the governing equations and in Section 3 the numerical method is explained in detail, including the high resolution scheme for convective fluxes and the various algorithm steps. In Section 4 a number of validation test cases are addressed to verify the correct implementation of the method and serve as validation. We start with two nearly incompressible flow test cases, namely the Shercliff and Hunt flow problems, which are intended to validate the method for low speed viscous and resistive MHD flows. In what regards ideal MHD validation, three standard bi-dimensional problems are addressed, namely the high density cloud shock wave interaction, the MHD rotor and MHD blast wave. Finally, in Section 5 we consider a more complex application case involving an MPD thruster, and in particular look into the effects of cathode geometry on the performance of a 2D self-field MPD thruster.

2. Governing equations

Magnetohydrodynamic is the area of physics in the intersection of fluid mechanics and electromagnetism which is concerned with the interaction of a conducting moving fluid with one or more magnetic fields. This interaction can be described by the MHD equations, which couple the magnetic field given by Maxwell equations, with the flow of a conducting fluid ruled by the Navier–Stokes equations. The resistive form of the MHD system of equations for an adiabatic electrical conducting fluid is given by:

$$\frac{\partial \rho}{\partial t} + \nabla \cdot (\rho \mathbf{U}) = 0, \quad (1)$$

$$\frac{\partial \rho \mathbf{U}}{\partial t} + \nabla \cdot \left[\rho \mathbf{U} \mathbf{U} + \left(p + \frac{\mathbf{B} \cdot \mathbf{B}}{2\mu_0} \right) \mathbf{I} - \frac{\mathbf{B} \mathbf{B}}{\mu_0} \right] = \nabla \cdot \boldsymbol{\tau}_{\text{visc}}, \quad (2)$$

$$\frac{\partial \rho e_t}{\partial t} + \nabla \cdot \left[\left(\rho e_t + p + \frac{\mathbf{B} \cdot \mathbf{B}}{2\mu_0} \right) \mathbf{U} - \mathbf{U} \cdot \frac{\mathbf{B}\mathbf{B}}{\mu_0} \right] = \nabla \cdot \left(\frac{\mathbf{B} \times \eta \mathbf{j}}{\mu_0} \right), \quad (3)$$

$$\frac{\partial \mathbf{B}}{\partial t} + \nabla \cdot (\mathbf{U}\mathbf{B} - \mathbf{B}\mathbf{U}) = -\nabla \times (\eta \mathbf{j}), \quad (4)$$

with the magnetic field subjected to Gauss law,

$$\nabla \cdot \mathbf{B} = 0. \quad (5)$$

This system expresses the conservation of mass (Eq. (1)), where ρ is the fluid density, momentum $\rho \mathbf{U}$, where \mathbf{U} is the velocity vector (Eq. (2)), total energy e_t (Eq. (3)), and propagation of the magnetic field \mathbf{B} (Eq. (4)). The plasma electrical resistivity is denoted by $\eta = 1/\sigma$, the permeability of free space is μ_0 and the electrical current density is \mathbf{j} . The viscous stress tensor for compressible Newtonian flow is given by:

$$\boldsymbol{\tau}_{visc} = -\left(\frac{2}{3}\mu \nabla \cdot \mathbf{U}\right) \mathbf{I} + \mu [\nabla \mathbf{U} + (\nabla \mathbf{U})^T], \quad (6)$$

where μ is the dynamic viscosity of the plasma. We note that the magnetic field contribution in both the momentum and energy equations acts as an equivalent magnetic stress tensor, which is traceless (in 2D), as the viscous stress tensor, and is formed by the dyadic product of $\mathbf{B}/\sqrt{\mu_0}$ by itself. As seen in Eqs. (2) and (3), the isotropic part of this magnetic stress can be grouped with the pressure p to form an equivalent global pressure $p + \mathbf{B} \cdot \mathbf{B}/(2\mu_0) = p + \frac{1}{2}B^2/\mu_0$. In the present algorithm the thermodynamic pressure, p , is calculated indirectly via an equation assembled using both the continuity (Eq. (1)) and the momentum (Eq. (2)) equations, following standard practices of pressure-correction algorithms. Temperature is a derived quantity and can be obtained from an equation of state,

$$T = \frac{1}{c_v} \left[e_t - \frac{1}{2} \left(\mathbf{U} \cdot \mathbf{U} + \frac{\mathbf{B} \cdot \mathbf{B}}{\rho \mu_0} \right) \right]. \quad (7)$$

Using Ampère's law and some standard vector identities, the last term of Eq. (4) can be rewritten in terms of \mathbf{B} :

$$\nabla \times (\eta \mathbf{j}) = \nabla \times \left(\eta \frac{\nabla \times \mathbf{B}}{\mu_0} \right) = -\nabla \cdot \left(\eta \nabla \frac{\mathbf{B}}{\mu_0} \right), \quad (8)$$

thus representing a diffusion-like contribution in the equation to be solved for \mathbf{B} (Eq. (4)). The electrical conductivity σ may either be specified as a constant value or is calculated as a scalar field of temperature and particle density using the Spitzer–Härm formulation [37],

$$\sigma = 1.53 \times 10^{-2} \frac{T^{3/2}}{\ln \Lambda}, \quad (9)$$

where,

$$\ln \Lambda = \ln \left(\frac{12\sqrt{2}\pi (k_B \epsilon_0 T)^{3/2}}{q^3 n^{1/2}} \right), \quad (10)$$

is the so-called Coulomb logarithm. In Eq. (10) k_B is the Boltzmann constant, q is the electron particle charge, ϵ_0 is the permittivity of free space and n is the particle density expressed in particles per cubic meter of plasma.

3. Pressure-based numerical method for multidimensional MHD

The method proposed follows the operator splitting ideas of the PISO algorithm (Issa [38,39]) to handle successive pressure and velocity corrections, in order to obtain a velocity field that satisfies simultaneously the continuity and the momentum equations. Here we need to bring also successive predictions and corrections of the magnetic field into the sequence of operations. In a previous effort [23] we have addressed the problem of the MHD equations under ideal flow and magnetic conditions. The same philosophy is now carried out for the compressible resistive MHD system of equations, whose solution is achieved via a sequence of segregated steps, of the PISO type, and with the global fluxes, including standard convection and magnetic effects being evaluated by an AUSM-type approach, as described below.

In order to improve accuracy and stability in the computation and resolution of the various types of MHD discontinuities we have adapted the AUSM-MHD flux scheme, originally proposed by Han et al. [12] in the framework of density-based solvers, to our pressure-correction method. The AUSM-MHD scheme is an improved version of the AUSMPW scheme [40] for ideal MHD, where the pressure-based weight functions were modified in order to account for the magnetic pressure. Another issue is that, in multidimensional MHD cases, one must ensure $\nabla \cdot \mathbf{B} = 0$ and for this purpose, the hyperbolic/parabolic divergence cleaning technique proposed by Dedner et al. [34] was incorporated in the present method. The code was developed within the Open Field Operation And Manipulation (OpenFOAM) CFD package. The OpenFOAM package is an object-oriented numerical simulation toolkit for continuum mechanics written in C++ language that is currently released by ESI Group.

3.1. Description of the algorithm

The pressure-based algorithm uses a segregated approach consisting of successive prediction and correction steps, with values obtained at a previous time step denoted with n , and consecutive predictions and corrections denoted with * , ** , *** . In the following subsections we have choose units for \mathbf{B} such that $\mu_0 = 1$ H/m. The convective fluxes are calculated with the AUSM-MHD method using the appropriate characteristic speed, $U \pm c$. The common fast magnetosonic speed at a control volume face, with left and right states denoted by indices L and R , is given by:

$$c_f = \min(c_L, c_R), \quad (11)$$

where,

$$c_{L,R} = \left\{ \frac{1}{2} \left[a_{L,R}^2 + \frac{B_{L,R}^2}{\rho_{L,R}} + \sqrt{\left(a_{L,R}^2 + \frac{B_{L,R}^2}{\rho_{L,R}} \right)^2 - 4a_{L,R}^2 \frac{B_{n,L,R}^2}{\rho_{L,R}}} \right] \right\}^{\frac{1}{2}}. \quad (12)$$

In Eq. (12) $a_{L,R}$ are the left and right states for the speed of sound and $B_n = \hat{\mathbf{S}}_f \cdot \mathbf{B}$ is the component of the magnetic field normal to the cell face.

3.1.1. Prediction step

In the first step of the algorithm we assume that the nodal values for the dependent variables are known from the previous time level n . We will then calculate the interpolation Mach number functions (\mathcal{M}_4^\pm , \mathcal{P}_5^\pm) that allows us to build the flux vectors for the three dimensional MHD equations,

$$\frac{\partial \mathcal{H}}{\partial t} + \nabla \cdot \mathcal{F}_f = \mathcal{S}, \quad (13)$$

where \mathcal{H} is the state vector for the conservative variables, the flux vectors for multidimensional MHD are given by \mathcal{F}_f and \mathcal{S} represents the diffusion and source terms contributions. These are given by:

$$\mathcal{H} = \begin{pmatrix} \rho \\ \rho U_x \\ \rho U_y \\ \rho U_z \\ B_x \\ B_y \\ B_z \\ \rho e_t \\ \Psi \end{pmatrix}, \quad \mathcal{S} = \begin{pmatrix} 0 \\ \nabla \cdot (\tau_{xx}, \tau_{yx}, \tau_{zx}) \\ \nabla \cdot (\tau_{xy}, \tau_{yy}, \tau_{zy}) \\ \nabla \cdot (\tau_{xz}, \tau_{yz}, \tau_{zz}) \\ \nabla \cdot (\eta \nabla B_x) \\ \nabla \cdot (\eta \nabla B_y) \\ \nabla \cdot (\eta \nabla B_z) \\ \nabla \cdot (\mathbf{B} \times \eta \nabla \times \mathbf{B}) \\ -\frac{c_h^2}{c_d^2} \Psi \end{pmatrix}, \quad (14)$$

$$\mathcal{F}_f = c_f (\mathcal{M}_4^+ \Phi_L^n + \mathcal{M}_4^- \Phi_R^n) + (\mathcal{P}_5^+ \mathbf{P}_L^n + \mathcal{P}_5^- \mathbf{P}_R^n) + \frac{1}{2} (\Phi_{B,L}^n + \Phi_{B,R}^n), \quad (15)$$

$$\Phi = \begin{pmatrix} \rho \\ \rho U_x \\ \rho U_y \\ \rho U_z \\ B_x \\ B_y \\ B_z \\ \rho e_t + p_G \\ 0 \end{pmatrix}, \quad \mathbf{P} = \begin{pmatrix} 0 \\ S_x p_G \\ S_y p_G \\ S_z p_G \\ -\bar{B}_f U_x \\ -\bar{B}_f U_y \\ -\bar{B}_f U_z \\ -\bar{B}_f (\mathbf{U} \cdot \mathbf{B}) \\ 0 \end{pmatrix}, \quad \Phi_B = \begin{pmatrix} 0 \\ -B_x \bar{B}_f \\ -B_y \bar{B}_f \\ -B_z \bar{B}_f \\ S_x \Psi \\ S_y \Psi \\ S_z \Psi \\ 0 \\ c_h^2 \bar{B}_f \end{pmatrix}. \quad (16)$$

Here, $p_G = p + \frac{B^2}{2}$ is the global pressure and $\bar{B}_f = (B_{f,L} + B_{f,R})/2$, where the magnetic flux at the face is $B_f = \sum S_i B_i$, with the subscript i representing the multiple components of the cell face area, \mathbf{S}_f , and \mathbf{B} vectors ($i = x, y, z$). The variable Ψ is a scalar field, c_h is a numerical speed enabling convection of errors associated with $\nabla \cdot \mathbf{B}$ and c_d is a dissipation coefficient that is responsible for the local damping of those same errors. These variables are related to the hyperbolic/parabolic divergence cleaning, see [34]. The scalar field Ψ is added to the magnetic field equation through a gradient term that enables the coupling between the $\nabla \cdot \mathbf{B} = 0$ constraint to the evolution equation for \mathbf{B} ,

$$\frac{\partial \mathbf{B}}{\partial t} + \nabla \cdot (\mathbf{UB} - \mathbf{BU}) + \nabla \Psi = \nabla \cdot (\eta \nabla \mathbf{B}). \quad (17)$$

An additional equations needs to be solved for Ψ ,

$$\frac{\partial \Psi}{\partial t} + c_h^2 \nabla \cdot \mathbf{B} = -\frac{c_h^2}{c_d^2} \Psi. \quad (18)$$

Where the velocity c_h and the dissipation coefficient c_d are determined by:

$$c_h = \frac{CFL}{\Delta t \times \max(\frac{1}{h})}, \quad (19)$$

$$CFL = \max \left[\frac{(|U_f| + c_f) \Delta t}{h} \right], \quad (20)$$

where h is the cell size and $U_f = c_f(\bar{\mathcal{M}}_4^+ + \bar{\mathcal{M}}_4^-)$ is the cell face velocity. Note that with this approach c_h is the maximum speed that is compatible with the CFL number. The dissipation coefficient is given by:

$$c_d = \sqrt{-\Delta t \frac{c_h^2}{\ln(C_r)}}, \quad \text{with } 0 < C_r < 1, \quad (21)$$

and in all calculations we set $C_r = 0.9$.

The PISO algorithm is a pressure-based method, which means that we need to calculate the thermodynamic pressure in a separated way,

$$p_f^n = \mathcal{P}_5^+ p_L^n + \mathcal{P}_5^- p_R^n. \quad (22)$$

Now the full system of equations is solved in a segregated way. The first equation to be solved is an explicit version of the continuity equation, based on the mass flux m_f that was previously assembled with the AUSM-MHD method (Eqs. (15) and (16), first line). The solution of this equation gives a prediction value for the density ρ^* ,

$$\frac{\partial \rho^*}{\partial t} + \nabla \cdot (m_f^n) = 0, \quad (23)$$

where the mass flux is,

$$m_f^n = c_f^n (\bar{\mathcal{M}}_4^+ \rho_L^n + \bar{\mathcal{M}}_4^- \rho_R^n). \quad (24)$$

Afterwards, an explicit equation for each component of the magnetic field is solved (following Eq. (17)),

$$\frac{\partial B_i^*}{\partial t} + \nabla \cdot (\mathcal{B}_f^n) = S_B, \quad (25)$$

$$\begin{aligned} \mathcal{B}_f^n = & c_f^n (\bar{\mathcal{M}}_4^+ B_{i,L}^n + \bar{\mathcal{M}}_4^- B_{i,R}^n) - \{ \mathcal{P}_5^+ [(\bar{B}_f)^n U_i^n]_L + \mathcal{P}_5^- [(\bar{B}_f)^n U_i^n]_R \} \\ & + \frac{1}{2} ([S_i \Psi^n]_L + [S_i \Psi^n]_R). \end{aligned} \quad (26)$$

Note that for 1D flows, with variations along the x -axis, in order to satisfy the $\nabla \cdot \mathbf{B} = 0$ condition we need to impose a constant value of B_x and just solve for B_y and B_z . Eq. (25) is based on fluxes that were calculated previously with the AUSM-MHD method (Eqs. (15) and (16), fifth, sixth and seventh lines) and their solution give us predicted values of B_x^* , B_y^* , and B_z^* . The Laplacian term (Eq. (8)) is calculated implicitly in conjunction with a fully implicit Euler scheme for time discretization, thus avoiding time step restriction related to an explicit representation of the diffusion term; the central differencing scheme is applied to discretize in space the second order derivative. For non-orthogonal grids, a correction is applied in the discretization of the Laplacian term, see Xisto et al. [21] for more details. Although here an implicit scheme has been applied for the viscous and resistive terms of the governing equations, it is worth mentioning that nowadays new methodologies are introduced that allow the method to remain fully explicit without the need of too small time steps, see the very recent papers by Meyer et al. [41,42] for more details.

The predicted velocity field, \mathbf{U}^* , is obtained by solving an explicit momentum equation for each direction,

$$\frac{\partial (\rho^* U_i^*)}{\partial t} + \nabla \cdot (\mathcal{U}_f^n) = -\nabla p_f^n + S_U, \quad (27)$$

with momentum flux:

$$\begin{aligned} \mathcal{U}_f^n = & c_f^n (\bar{\mathcal{M}}_4^+ [\rho^* U_i^n]_L + \bar{\mathcal{M}}_4^- [\rho^* U_i^n]_R) + \left\{ \mathcal{P}_5^+ \left[S_i \frac{(\mathbf{B} \cdot \mathbf{B})^*}{2} \right]_L + \mathcal{P}_5^- \left[S_i \frac{(\mathbf{B} \cdot \mathbf{B})^*}{2} \right]_R \right\} \\ & - \frac{1}{2} \{ [(\bar{B}_f)^n B_i^*]_L + [(\bar{B}_f)^n B_i^*]_R \}. \end{aligned} \quad (28)$$

The pressure gradient and the magnetic field terms are treated in an explicit way using the predicted magnetic field values B_x^* , B_y^* , B_z^* (from Eq. (25)) and the previously calculated face values of pressure, Eq. (22). The discretized momentum equation for \mathbf{U}^* , from Eq. (27), is given by,

$$a_p^u \mathbf{U}^* = \mathbf{H}(\mathbf{U}^n) - \nabla p_f^n, \quad (29)$$

where a_p^u is the central velocity coefficient and the operator $\mathbf{H}(\mathbf{U}^n)$ is built using convection and diffusion coefficients terms of neighbor cells to P , and adding the magnetic explicit terms (related to the magnetic stress in Eq. (2)) and the explicit part of the time derivative discretization:

$$\mathbf{H}(\mathbf{U}^n) = \sum a_N^U \mathbf{U}_N^n + S_B^* + \frac{\rho^* \mathbf{U}^n V_P}{\Delta t}, \quad (30)$$

where V_P is the geometrical volume of cell P . In order to remove any time step restrictions induced by explicit representations, the second order viscous term in the newtonian stress (Eq. (6)) is represented implicitly with the central differencing scheme based on new time velocity values.

The last equation to be solved, before the PISO correction cycle, is an equation for the conservation of total energy,

$$\frac{\partial(\rho^* e_t^*)}{\partial t} + \nabla \cdot (\mathcal{E}_f^n) = S_e, \quad (31)$$

with the energy flux:

$$\begin{aligned} \mathcal{E}_f^n = & c_f^n \left\{ \bar{\mathcal{M}}_4^+ \left[\rho^* e_t^n + \frac{(\mathbf{B} \cdot \mathbf{B})^*}{2} + p^n \right]_L + \bar{\mathcal{M}}_4^- \left[\rho^* e_t^n + \frac{(\mathbf{B} \cdot \mathbf{B})^*}{2} + p^n \right]_R \right\} \\ & - \{ \mathcal{P}_5^+ [(\bar{B}_f)^n (\mathbf{U}^* \cdot \mathbf{B}^*)]_L + \mathcal{P}_5^- [(\bar{B}_f)^n (\mathbf{U}^* \cdot \mathbf{B}^*)]_R \}. \end{aligned} \quad (32)$$

We note that the total energy flux together with the contribution of thermodynamic and magnetic pressures are interpolated by the fourth order Mach number interpolation function, while the magnetic stress is interpolated by the fifth order Mach number interpolation function. The second order terms on the right side are calculated explicitly using again the central-differencing scheme. Afterwards, the temperature field, T , is updated using the correspondent equation of state,

$$T^* = \frac{1}{c_v} \left[e_t^* - \frac{1}{2} \left\{ (\mathbf{U} \cdot \mathbf{U})^* + \frac{(\mathbf{B} \cdot \mathbf{B})^*}{\rho^*} \right\} \right]. \quad (33)$$

With this new temperature, updated values for the compressibility coefficient are evaluated, $\psi^* = 1/RT^*$, and density can also be updated, $\rho^{**} = \psi^* p^n$.

3.1.2. Correction step

The $\mathbf{H}(\mathbf{U}^n)$ operator in Eq. (29) gives an intermediate velocity field which does not take into account the effect of pressure. Mach number interpolation functions are evaluated once again inside the PISO cycle, with the AUSM-MHD method. These new functions are applied to calculate the sonic flux which is required in the pressure equation,

$$F_s^* = c_f^* (\bar{\mathcal{M}}_4^+ \psi_L^* + \bar{\mathcal{M}}_4^- \psi_R^*). \quad (34)$$

Then, the pressure equation is built and solved, using the previously obtained values for compressibility, ψ^* , and density, ρ^{**} , as:

$$\frac{\partial(\psi^* p^*)}{\partial t} + \nabla \cdot (F_s^* p^*) - \nabla \cdot \left(\frac{\rho^{**}}{a_p^u} \nabla p^* \right) = 0, \quad (35)$$

thus giving the predicted values for a new pressure field, p^* . The velocity field is corrected in an explicit way using the new pressure gradient and the first predicted velocity. The pressure gradient is again calculated with the pressure face value obtained with the Mach number interpolation functions,

$$\mathbf{U}^{**} = \frac{\mathbf{H}(\mathbf{U}^n) - \nabla p_f^*}{a_p^u}. \quad (36)$$

Finally, density is corrected using the equation of state $\rho^{***} = \psi^* p^*$. This cycle should be repeated until the momentum and continuity equations are satisfied simultaneously and, in all calculations, we have used two correction steps as is typical in the PISO algorithm. It is noted that at the end of a correction step, the mass fluxes based on velocity \mathbf{U}^{**} and density ρ^{***} satisfies the continuity equation (Eq. (35)) exactly, and therefore mass conservation is guaranteed at every control volume and in the entire domain.

3.1.3. Summary of the algorithm steps

The different steps of the algorithm can now be summarized:

1. All nodal values are either assumed to be known at the old time level n or are estimated at the beginning of the computation.
2. The interpolation Mach number-based functions $\bar{\mathcal{M}}_4^\pm$ and \mathcal{P}_5^\pm are calculated and the flux vectors for the multidimensional MHD equations are assembled.
3. Predictor values for density ρ^* and for each component of the magnetic field B_i^* are determined from Eqs. (23) and (25), respectively.
4. A prediction of the velocity field U_i^* is obtained from Eq. (27), the pressure gradient and magnetic field terms are also treated in an explicit way using the predicted magnetic field values B_i^* and the previously corrected value of pressure p^n .
5. Total energy is predicted with Eq. (31) and temperature T^* is then explicitly obtained from the equation of state (33), where the terms of magnetic and kinetic energy were calculated with the previously predicted values of velocity and magnetic fields. Compressibility is estimated, $\psi^* = 1/(RT^*)$, and density is updated $\rho^{**} = \psi^* p^n$.
6. The PISO cycle begins. The $\mathbf{H}(\mathbf{U}^n)$ operator is built and an intermediate velocity, which does not take into account the pressure gradient, is calculated $\hat{\mathbf{U}}^* = \mathbf{H}(\mathbf{U}^n)/a_p^u$.
7. The Mach number interpolation functions are calculated once again inside PISO and the sonic flux is assembled, (Eq. (34)).
8. The pressure equation (Eq. (35)) is assembled with the sonic flux and solved in order to give us a predicted value for pressure, p^* . The velocity field is finally corrected, U^{**} , in an explicit way using Eq. (36). The final step of PISO cycle gives us a correction of density, ρ^{***} using an equation of state.
9. This PISO cycle should be repeated until momentum and continuity are satisfied, therefore the continuity equation is introduced inside the cycle. It is possible to check convergence within a time step by monitoring a mass conservation error with mass fluxes based on velocity predictions \mathbf{U}^* (from step 4) and density ρ^{**} (from step 5).

3.2. Interpolation functions

Interpolation functions depending on the local combined sonic and magnetic Mach number, are required to obtain face values of the fluxes for the corresponding values of the left and right states. These functions are described in detail in previous works [12,21,23,43] and so it suffices to give here their expressions:

$$\mathcal{M}_{(4)}^\pm(M) = \begin{cases} \mathcal{M}_{(2)}^\pm(M)(1 \mp 16\beta\mathcal{M}_{(2)}^\mp(M)) & |M| < 1 \\ \mathcal{M}_{(1)}^\pm(M), & |M| \geq 1 \end{cases} \quad (37)$$

and,

$$\mathcal{P}_{(5)}^\pm(M) = \begin{cases} \mathcal{M}_{(2)}^\pm(M)[(\pm 2 - M) \mp 16\alpha M\mathcal{M}_{(2)}^\mp(M)], & |M| < 1 \\ \frac{1}{M}\mathcal{M}_{(1)}^\pm(M) & |M| \geq 1 \end{cases} \quad (38)$$

with

$$\mathcal{M}_{(1)}^\pm(M) = \frac{1}{2}(M \pm |M|), \quad (39)$$

$$\mathcal{M}_{(2)}^\pm(M) = \pm \frac{1}{4}(M \pm 1)^2. \quad (40)$$

The global-pressure-based weight functions are now introduced for accounting the magnetic effects and pressure fluctuations in the interpolation functions:

$$M_f = \mathcal{M}_4^+ + \mathcal{M}_4^- \geq 0:$$

$$\begin{aligned} \bar{\mathcal{M}}_4^- &= \mathcal{M}_4^- \cdot w \cdot (1 + f_R), \\ \bar{\mathcal{M}}_4^+ &= \mathcal{M}_4^+ + \mathcal{M}_4^- \cdot [(1 - w) \cdot (1 + f_R) - f_L], \end{aligned} \quad (41)$$

$$M_f = \mathcal{M}_4^+ + \mathcal{M}_4^- < 0:$$

$$\begin{aligned} \bar{\mathcal{M}}_4^+ &= \mathcal{M}_4^+ \cdot w \cdot (1 + f_L), \\ \bar{\mathcal{M}}_4^- &= \mathcal{M}_4^- + \mathcal{M}_4^+ \cdot [(1 - w) \cdot (1 + f_L) - f_R], \end{aligned} \quad (42)$$

where f and w are functions of the global pressure defined by:

$$f_{L,R} = \begin{cases} \left(\frac{p_{G,L} + p_{G,R}}{p_{G,s}} - 1 \right), & p_{G,s} \neq 0, \\ 0, & p_{G,s} = 0, \end{cases} \quad p_{G,s} = \mathcal{P}_5^+ p_{G,L} + \mathcal{P}_5^- p_{G,R}, \quad (43)$$

$$w = 1 - \min \left(\frac{p_{G,L}}{p_{G,R}}, \frac{p_{G,R}}{p_{G,L}} \right)^3, \quad (44)$$

with

$$p_{G,L} = p_L + \frac{1}{2} (B_x^2 + B_y^2 + B_z^2)_L, \quad (45)$$

$$p_{G,R} = p_R + \frac{1}{2} (B_x^2 + B_y^2 + B_z^2)_R. \quad (46)$$

The Mach number, M , is calculated with the fast magnetosonic speed,

$$M_{L,R} = \frac{U_{L,R}}{c_f}. \quad (47)$$

3.3. High resolution differencing scheme

For variable interpolation a high resolution scheme, namely the CUBISTA (Convergent and Universally Bounded Interpolation Scheme for Treatment of Advection) was included in the current numerical model. This scheme was devised by [44] in order to improve the iterative convergence properties, while retaining accuracy. It is based on QUICK (Quadratic Upstream Interpolation for Convective Kinetics) and it is composed by three segments: a TVD limiter on the left, $\psi(r) = 3r/2$, and a TVD limiter on the right, $\psi(r) = 3/2$. The implementation of this scheme in the NVD diagram is the following:

$$\tilde{\phi}_f = \begin{cases} \frac{7}{4}\tilde{\phi}_P & 0 < \tilde{\phi}_P < \frac{3}{8} \\ \frac{3}{4}\tilde{\phi}_P + \frac{3}{8} & \frac{3}{8} \leq \tilde{\phi}_P \leq \frac{3}{4} \\ \frac{1}{4}\tilde{\phi}_P + \frac{3}{4} & \frac{3}{4} \leq \tilde{\phi}_P \leq 1 \\ \tilde{\phi}_P & \text{elsewhere.} \end{cases} \quad (48)$$

Where $\tilde{\phi}$ is the normalized variable on the cell face, f , and cell center P .

3.4. Thruster parameters

We have used several parameters to assess the performance of the MPD thruster addressed in Section 5. The overall thrust force is computed from the momentum flux at thruster exit,

$$F = \int_{out} (\rho U^2 + p) dS. \quad (49)$$

The volume integral of the axial component of the Lorentz force gives the electromagnetic (ELM) component of the overall propulsion force,

$$F_{ELM} = \int_V (\mathbf{j} \times \mathbf{B})_x dV. \quad (50)$$

The thermal contribution is easily obtained as the difference between total and ELM forces,

$$F_{Therm} = F - F_{ELM}, \quad (51)$$

and the thruster specific impulse can then be computed as:

$$I_{spec} = \frac{F}{\dot{m}g_0}, \quad (52)$$

where $g_0 = 9.8 \text{ m/s}^2$ represents acceleration due to gravity and \dot{m} is the mass flow rate. From Eq. (52) we can conclude that a system producing a higher specific impulse is more efficient since it can generate more thrust for the same mass of gas propellant. The efficiency of a self-field 2D MPD thruster is thus given by [45]

$$\vartheta_{eff} = \frac{F^2}{2\dot{m}I(V + V_{elet})}, \quad (53)$$

where V and V_{elet} are electrical potential differences and I is the discharge current. The electrical voltage across the plasma, V , can be calculated as the line integral of Ohm's law from anode to cathode,

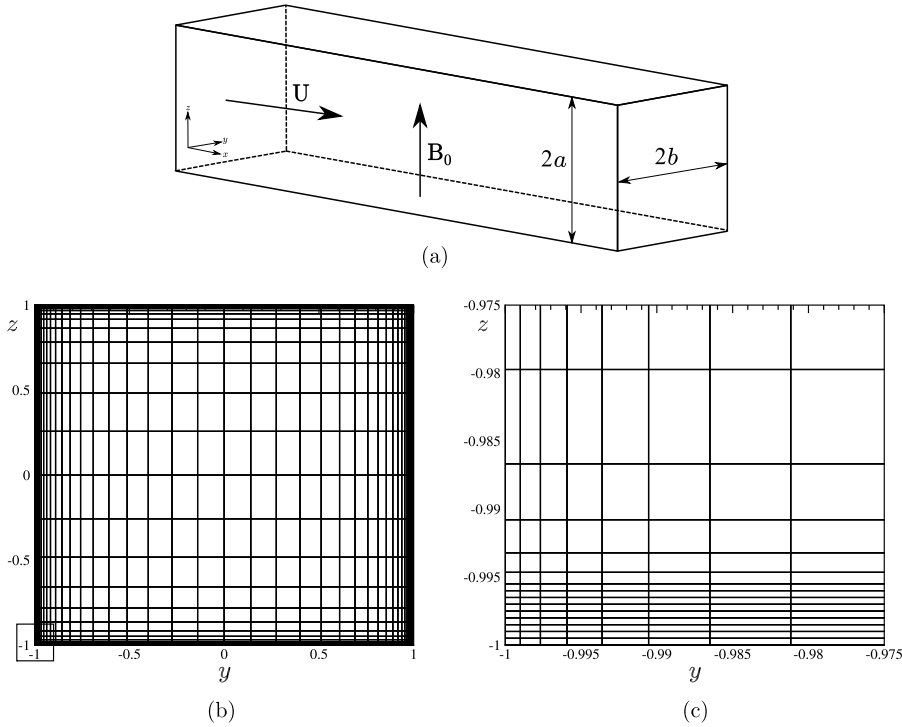


Fig. 1. (a) Geometry used for the channel flow problem. Global (b) and detailed view (c) of the numerical grid.

$$V = \int \mathbf{E} \cdot d\mathbf{l} = \int (\eta \mathbf{j} - \mathbf{U} \times \mathbf{B}) \cdot d\mathbf{l}. \quad (54)$$

The numerical model is not able to predict the potential drop due to electric sheath formation near the electrode walls. For that reason a constant value of $V_{\text{elet}} = 20$ V was specified [45,46].

4. Validation

In the following subsections we validate the method described in Section 3 under conditions that involve resistive and ideal MHD flows. Five test cases are addressed, starting with the two well-known Shercliff and Hunt flow problems, which are adequate to check the method in low speed resistive MHD viscous flow. The three remaining cases are standard 2D ideal MHD problems, which are useful to assess the method in flows exhibiting complex MHD shock interaction.

4.1. Resistive MHD validation

The first set of test cases to be used for validation are related to resistive MHD viscous flow. These problems comprise the flow of an electrical conducting fluid with finite electrical resistivity which is driven by a constant pressure gradient in a duct channel. Afterwards the flow is subjected to an applied magnetic field which is imposed in the perpendicular direction to the fluid movement, see Fig. 1(a). The cross section of the channel is in general rectangular, with a width equal to $2b$ and height equal to $2a$, but in both test cases we have assumed $a = b = 1$. The magnetic field is applied in the direction parallel to wall $2a$ (along z) and the flow direction is along the x -axis. Although this is a 3D flow problem, it can be converted into a two-dimensional problem if we only consider one cross-section of the channel with periodic boundary conditions applied along the flow direction. Under this simplified configuration, two distinct problems can be stated, differing from each other only in the type of wall boundary conditions for the magnetic field, namely the Shercliff [47] and Hunt [48] problems.

4.1.1. Shercliff flow problem

We consider first the Shercliff flow problem, in which case the channel is composed by four electrical insulating walls. Following the same approach as Ni et al. [49], we have chosen values for the magnetic field, electrical resistivity and dynamic viscosity that result in a Hartmann number ($Ha = B_0 L \sqrt{1/\eta\mu}$, L is the characteristic length) equal to $Ha = 1000$ and a Reynolds number $Re = 10$. The constant pressure gradient ($(\nabla p)_x = -102.88$ Pa/m) was calculated from Shercliff's analytical solution and results in a mass flow rate equal to 4 kg/s. For the numerical solution of the Shercliff problem a 2D $N \times N$ non-uniform grid with $N = 46$ was used, see Fig. 1(b). In Fig. 1(c) a zoomed view of the numerical mesh in the lower left corner is presented. It is worth noting that the different level of refinement along y and z is related to the two

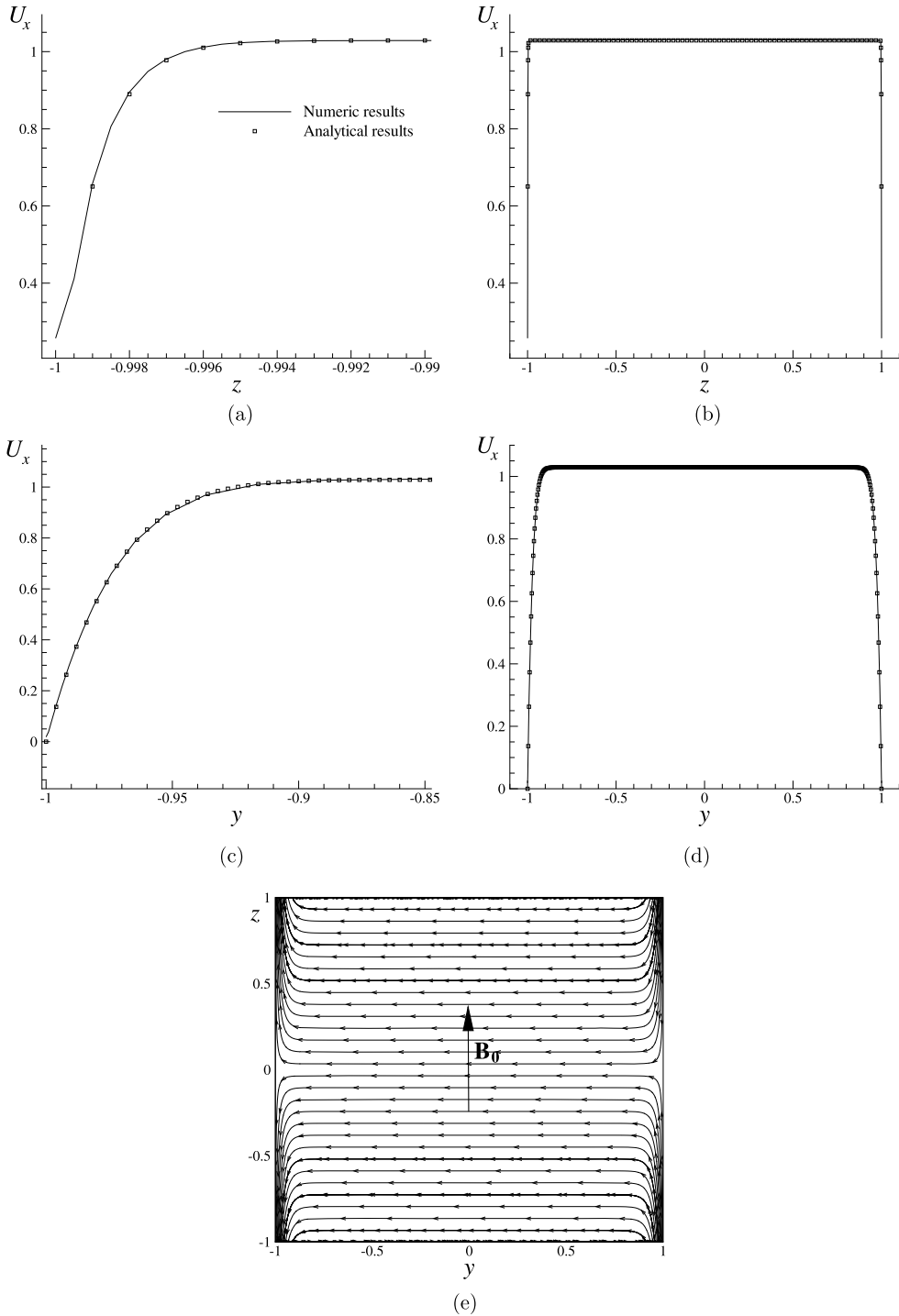


Fig. 2. Comparison between numerical and analytical results for the Shercliff test case: (a) Hartmann boundary layer; (b) Velocity profile in the middle $y = 0$ section; (c) Shercliff boundary layer; (d) Velocity profile in the middle $z = 0$ section; (e) Electric current lines.

distinct boundary layer thickness. It is known that the thickness of the Hartmann boundary layer, formed between the top and bottom walls, along the direction of the applied magnetic field, is proportional to Ha^{-1} , so we need more points in the z direction. The so-called Shercliff boundary layer, perpendicular to the \mathbf{B}_0 and \mathbf{U} plane, has a thickness proportional to $Ha^{1/2}$, which means that less points are required in the y direction.

In Fig. 2 we present a comparison between the analytical and numerical results, where the analytical solution was obtained with the exponential equations of Ni et al. [49]. It is clear that our numerical MHD model can predict with

some accuracy the thickness of both boundary layers, at the side walls ($y = \pm 1$, Shercliff layer) and at the top/bottom walls ($z = \pm 1$, Hartmann layer); in these zones enlarged scales are employed to highlight the near-wall velocity profiles. In Fig. 2(e) we present the computed electric current lines. Notice how current lines are almost parallel to the applied magnetic field in the Shercliff layer at $y = \pm 1$. This is the main reason for the distinct boundary layer thickness, since in these regions the axial component of the Lorentz force, $-B_z j_y$, is significantly reduced.

4.1.2. Hunt flow problem

The Hunt problem is another well known test case for incompressible resistive MHD viscous flow. For this problem the channel is composed by two electrical insulated walls, placed parallel to the applied magnetic field (in this case B_z), and two conducting walls perpendicular to the applied field, see Fig. 1(a). We consider again a fully developed flow with a Reynolds number equal to $Re = 10$ but in this case the variables are chosen so that the Hartmann number becomes $Ha = 300$. As in the previous case the flow is unidirectional along the x direction but it is now driven by a constant pressure gradient value of -300 Pa/m. For the conducting walls an electrical conductance ratio $(\sigma_w \cdot t_w / (\sigma \cdot a))$, where σ_w is the wall conductivity and t_w is the wall thickness) equal to 0.1 is specified. The analytical solution can be evaluated with the hyperbolic functions as originally proposed by Hunt [48] or, alternatively, with an exponential version of those equations that was suggested by Ni et al. [49].

In Fig. 3 we present a comparison between the analytical solution and the numerical results. We see that, for both the sidewalls and the Hartmann boundary layers, the numerical results agree reasonably well with the analytical solution, with some slight disagreement in intersection between the wall and flow core layers. The side-wall jets (Fig. 3(a)) are formed by the in-balance between the pressure gradient and the Lorentz force. Close to these insulated walls the current lines are parallel to the applied magnetic field, and thus the electromagnetic braking force is significantly reduced, see Fig. 3(e). As a consequence the pressure gradient in these region is mainly balanced by the viscous force alone and the flow protrudes through the magnetic field in thin jets along the side-walls [50].

4.2. Ideal MHD validation

Three standard problems involving only the ideal version of the MHD model are tackled in this section, namely the cloud–shock interaction, the MHD rotor and the MHD blast wave. In these two-dimensional MHD simulations we have chosen units for \mathbf{B} such that the vacuum magnetic permeability (μ_0) becomes equal to unity.

4.2.1. Cloud–Shock interaction

The first test case is related to a well-known problem in astrophysics, see [51]. It comprises the interaction between a strong shock wave and a high density cloud while subjected to a given initial magnetic field. The computational domain is a square box with $x, y \in [0; 1]$ which is discretized with three successively refined $N \times N$ uniform grids ($N = 200$, $N = 400$ and $N = 800$). The initial conditions, which are presented in Fig. 4(a), show a discontinuity parallel to the y axis that lies at $x = 0.6$ with the following left and right states for the dependent variables:

$$\begin{bmatrix} \rho \\ U_x \\ U_y \\ U_z \\ p \\ B_x \\ B_y \\ B_z \end{bmatrix} = \begin{bmatrix} 3.86859 \\ 0 \\ 0 \\ 0 \\ 167.345 \\ 0 \\ 2.18262 \\ -2.18262 \end{bmatrix}_L = \begin{bmatrix} 1 \\ -11.2536 \\ 0 \\ 0 \\ 1 \\ 0 \\ 0.564190 \\ 0.564190 \end{bmatrix}_R. \quad (55)$$

In this problem the adiabatic index is equal to $\gamma = 5/3$ and ideal MHD conditions are achieved by setting the fluid electrical resistivity to zero. Initially, the high density cloud has $\rho = 10$ and assumes a circular shape with centre at $(x, y) \in (0.8; 0.5)$ and radius equal to 0.15. The value of pressure inside and outside the circular cloud is $p = 1$, so the cloud is in hydrostatic equilibrium with the environment and will not deform itself without being subjected to an external body force. Regarding the boundary conditions, due to supersonic flow, the right side of the square box is an inlet where all variables are prescribed by the fixed right-side values given in Eq. (55), and in the remaining boundaries the variables are extrapolated from the inside of the solution domain.

The results presented were obtained for a final time of $t = 0.06$, before the cloud leaves the numerical domain. In Fig. 4(b) we present the contour plots for density in a logarithmic gray scale and in Figs. 4(c), 4(d) and 4(e) the magnetic field lines predicted on the three grids are plotted. By comparing these plots we see that the discontinuities are computed with a good resolution for all the grid dimensions N and no unrealistic flow patterns are observed even with the coarser grid. We note that this problem does not have a known analytical solution and therefore assessment can only be done by comparing our results against numerical results obtained by other authors, see [51,52].

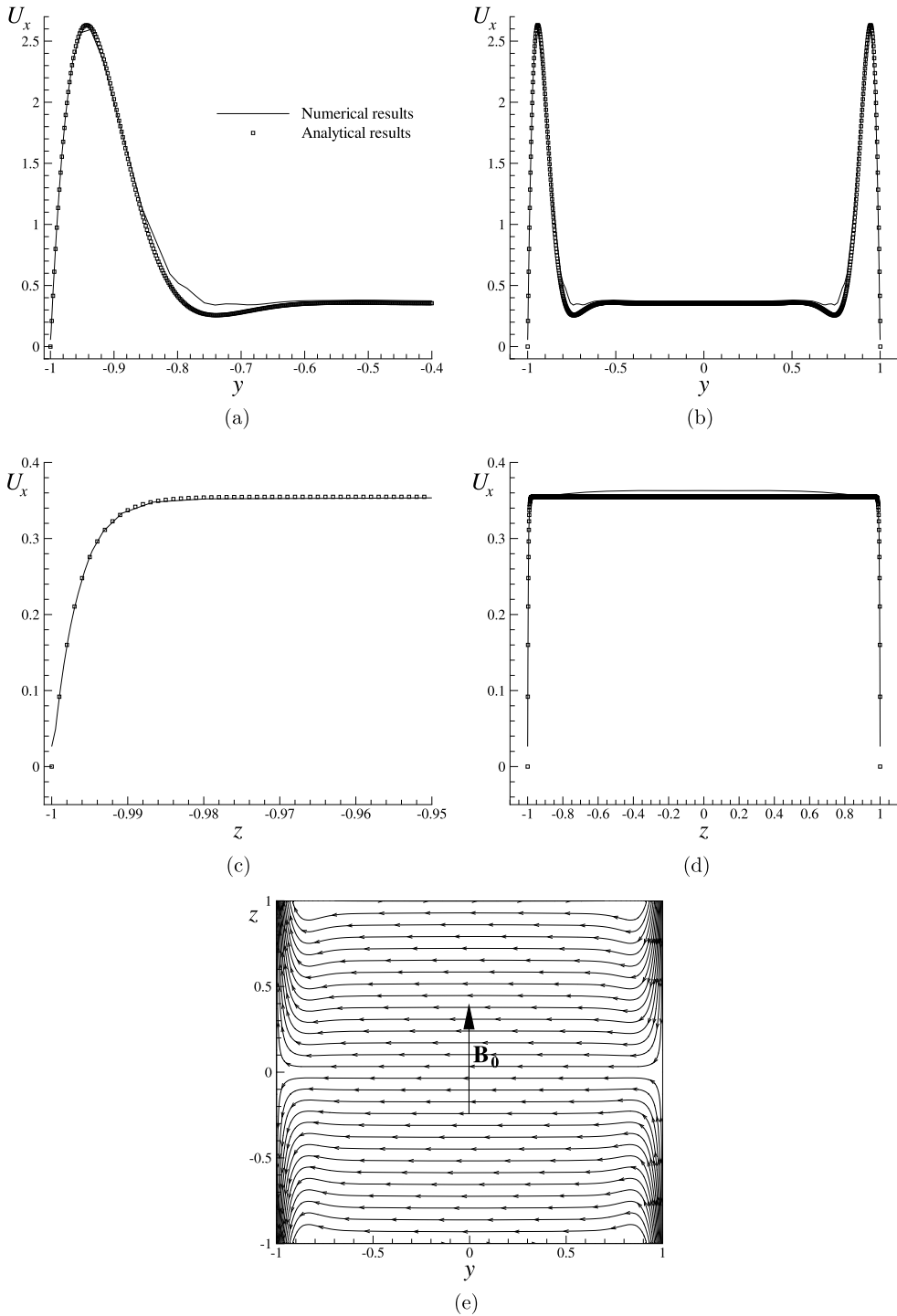


Fig. 3. Comparison between numerical and analytical results for the Hunt flow test case: (a) Side-wall boundary layer; (b) Velocity profile in the middle $z = 0$ section; (c) Hartmann boundary layer; (d) Velocity profile in the middle $y = 0$ section; (e) Electric current lines.

The unsteady solution computed with the $N = 200$ grid is presented in Fig. 5. We can see that the cloud is only deformed by its interaction with the strong shock wave. The solution seems to run smoothly even at the instance of collision.

In Table 1 we register a measure of the discretization error calculated as the relative difference of the pressure field in relation to a reference solution obtained on the finest grid,

$$\delta p_{\text{ref}} = \frac{\sum |p - p_{\text{ref}}|}{\sum p_{\text{ref}}}. \quad (56)$$

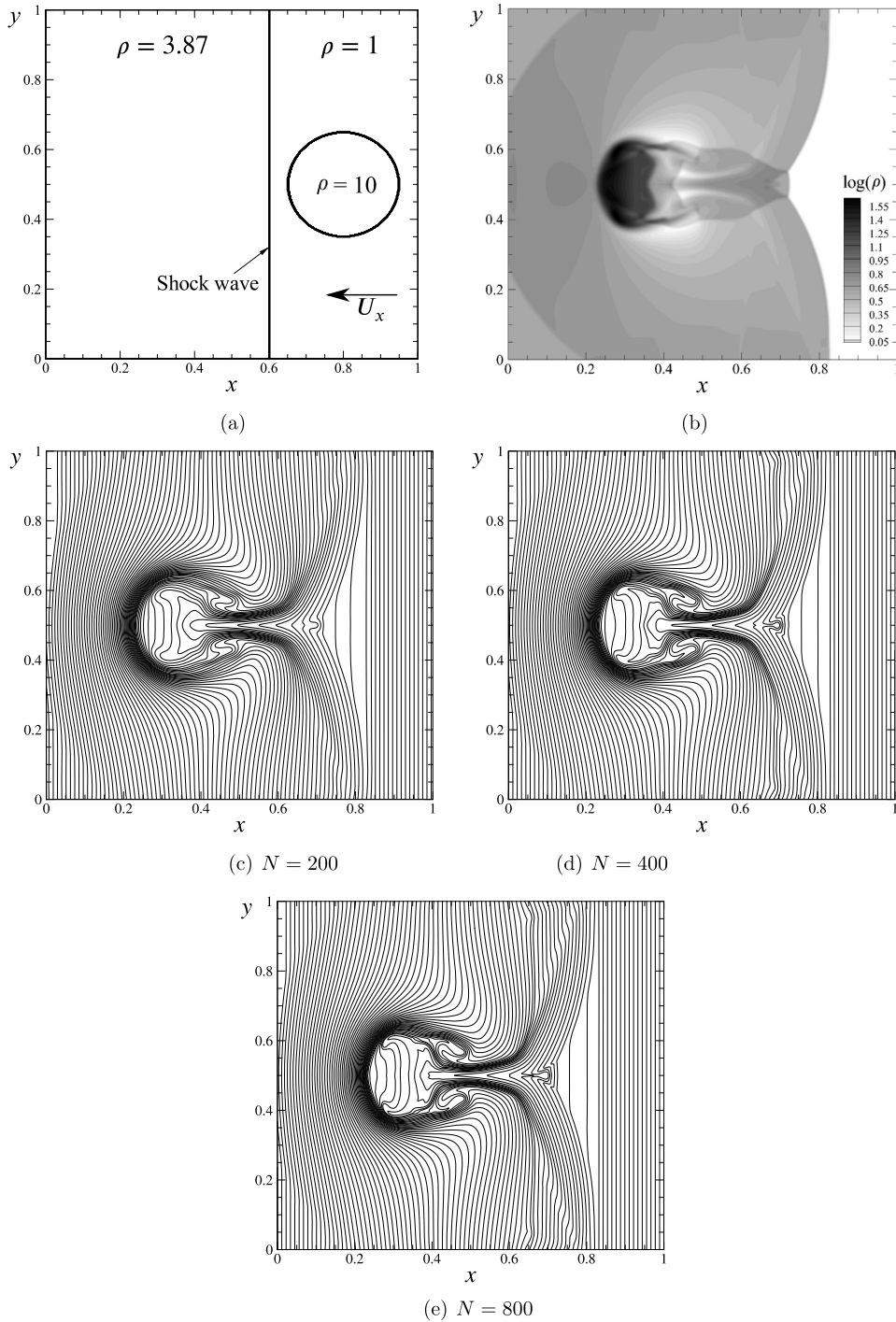


Fig. 4. Results obtained for the cloud-shock interaction test case. (a) Initial conditions for density. (b) Solution for density in a gray log scale after $t = 0.06$ ($N = 400$). Magnetic field lines computed at $t = 0.06$ in the three grids: $N = 200$ (c); $N = 400$ (d); $N = 800$ (e).

In order to evaluate the pressure difference in Eq. (56) we have interpolated the pressure distribution from the coarser meshes into the finer mesh and the summation is taken over the entire domain, with p_{ref} calculated on the most refined mesh ($N = 800$). δp_{ref} is plotted as a function of mesh spacing, under log-log scale, in Fig. 10(a) demonstrating that the proposed method achieves a convergence rate in space that is between the first and second order grid convergence slopes. In this flow, second order convergence is not actually achieved because we are in the presence of MHD discontinuities and the TVD limiters act in such a way that tend to reduce the formal order of the method, for the sake of stability.

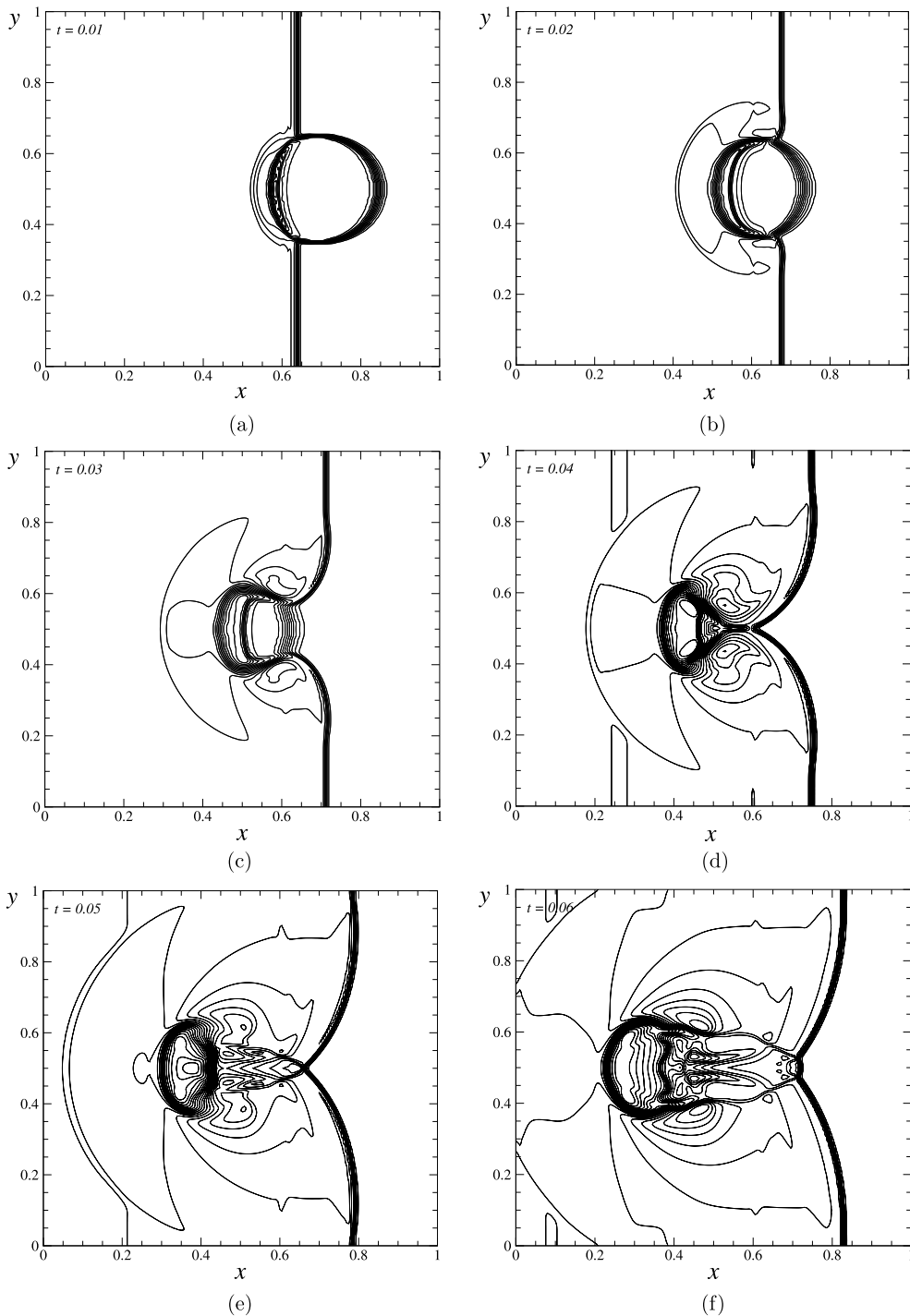


Fig. 5. Unsteady solution for the cloud-shock interaction shows density contour plots in the time range 0–0.06 on the $N = 200$ grid.

4.2.2. MHD rotor

The second test case here employed for MHD validation under ideal non-resistive conditions is the so-called MHD rotor. This two-dimensional problem consists of a rotating cylinder with density ten times superior to that of the surrounding environment. It was first formulated by Balsara and Spicer [53] and allows assessment of the numerical methodology for the calculation of torsional Alfvén waves. The rotation speed is an initial condition of the problem and no other external forces are applied to the rotor. At the initial time instance ($t = 0$) the cylinder and the environmental fluid are subjected to a uniform and uni-directional magnetic field. This problem is solved in a square domain $x, y \in [0; 1]$ with three uniform

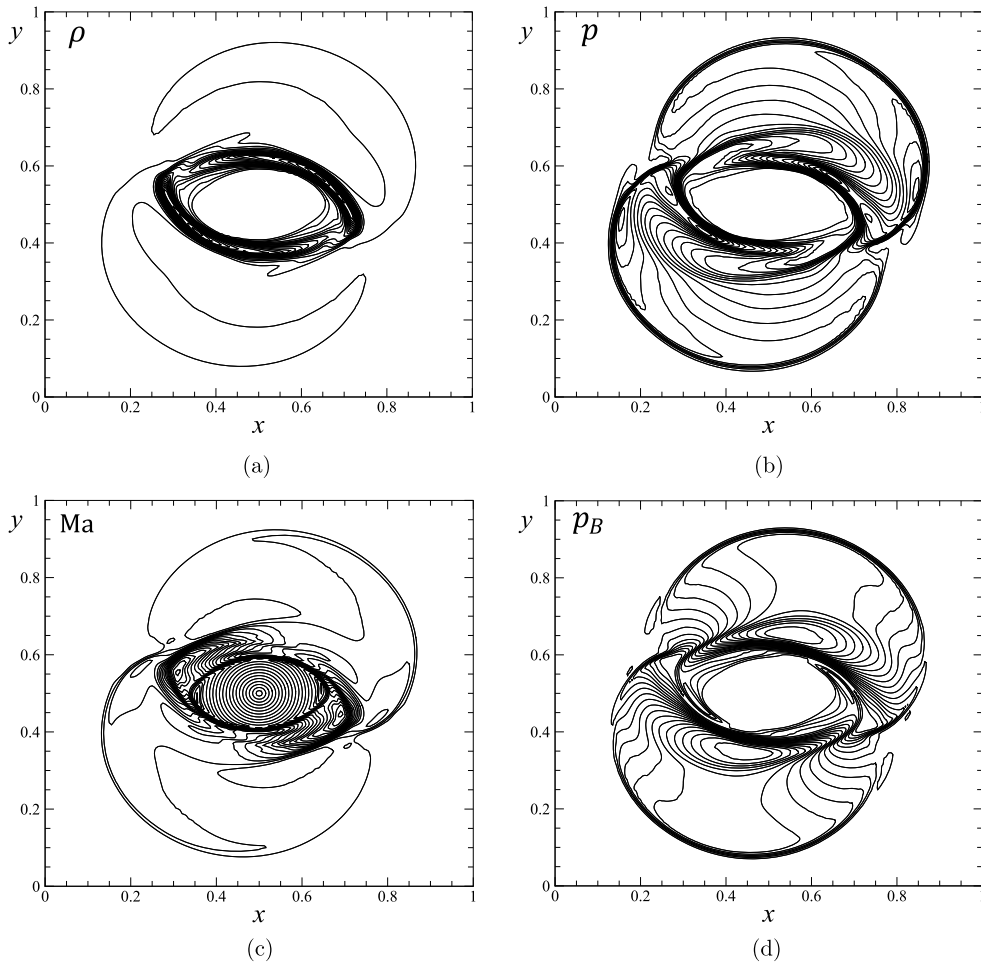


Fig. 6. Numerical results for the MHD rotor with the $N = 200$ grid at $t = 0.15$; contour plots of: density (a); thermodynamic pressure (b); Mach number (c); and magnetic pressure (d).

grids having the same number of grid points along x and y ($N = 200$, $N = 400$ and $N = 800$). The initial conditions for the magnetic field and thermodynamic pressure are uniform,

$$B_y = 0; \quad B_x = 5/\sqrt{4\pi}; \quad p = 1; \quad \gamma = 1.4. \quad (57)$$

Since this is an ideal MHD problem, the electric resistivity is assumed to be zero. The initial conditions for the rotating cylinder of radius $r_0 = 0.1$, centered at $(x, y) = (0.5, 0.5)$, are the following:

$$\rho = 10; \quad U_x = -U_0 \frac{(y - 0.5)}{r_0}; \quad U_y = U_0 \frac{(x - 0.5)}{r_0}. \quad (58)$$

Notice that U_x and U_y are functions of the radial distance from the initial cylinder center position $r < r_0$, with $r = [(x - 0.5)^2 + (y - 0.5)^2]^{1/2}$, and the dimensionless speed at the periphery of the cylinder is $U_0 = 2$. The environment is stationary ($U_x = U_y = 0$) with a density ($\rho = 1$) ten times lower than inside the cylinder and is defined by the region $r > r_1$ ($r_1 = 0.115$). In order to obtain a soft transition between the rotating cylinder and the environmental fluid another region was created, with linear profiles for density and velocity,

$$\rho = 1 + 9f; \quad U_x = -fU_0 \frac{(y - 0.5)}{r}; \quad U_y = fU_0 \frac{(x - 0.5)}{r}; \quad (59)$$

where,

$$f = (r_1 - r)/(r_1 - r_0). \quad (60)$$

For the two first grids having $N = 200$ and $N = 400$ we have used the CUBISTA interpolation scheme. However, due to convergence problems, for the most refined grid ($N = 800$) the Minmod limiter was used instead.

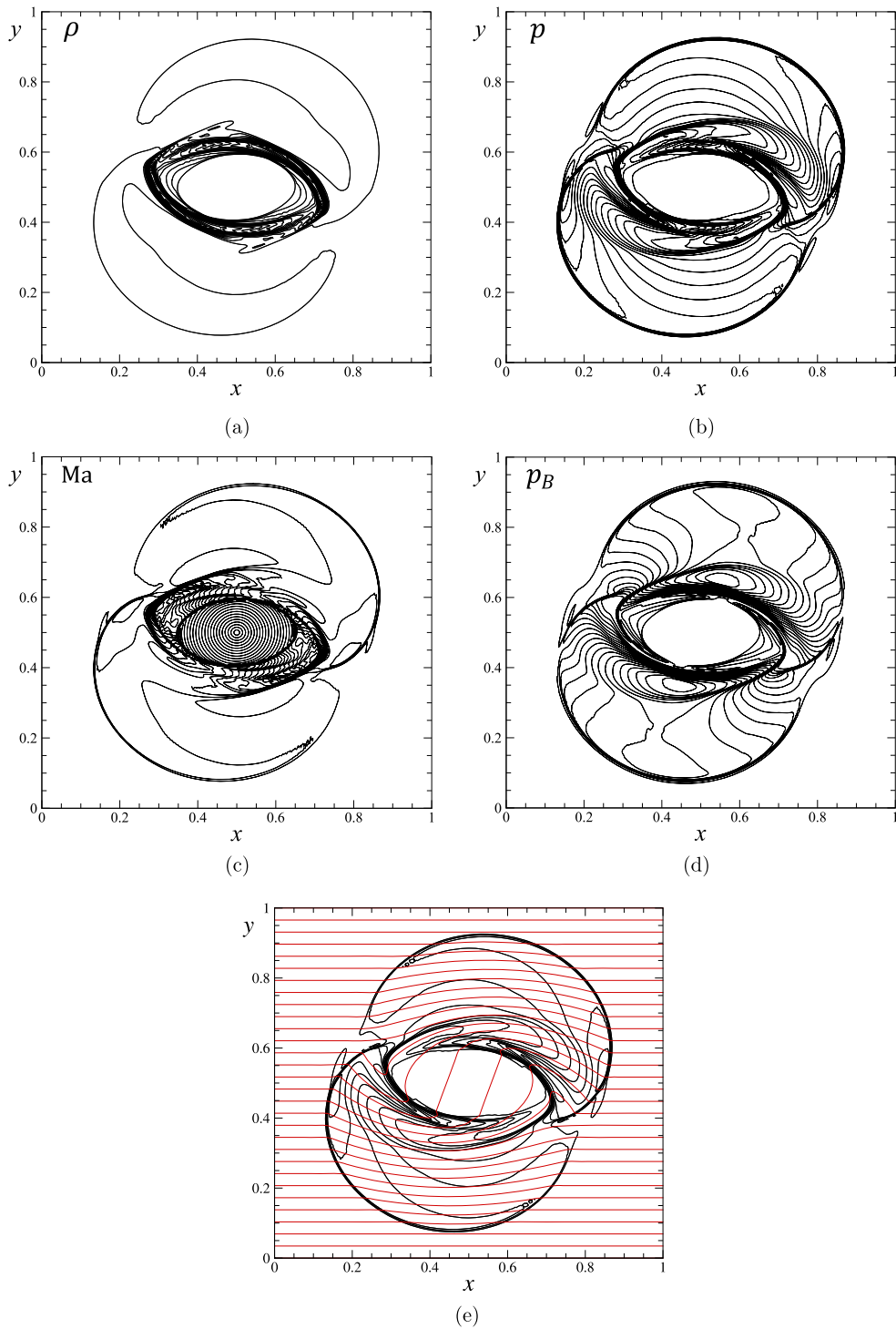


Fig. 7. Numerical results for the MHD rotor with the $N = 400$ grid at $t = 0.15$; contour plots of: density (a); thermodynamic pressure (b); Mach number (c); and magnetic pressure (d). (e) Magnetic field lines.

In Figs. 6, 7 and 8 we present the results obtained at $t = 0.15$, before the torsional waves reach the computational domain boundary and after the cylinder has completed about half a full rotation. These plots show contours of: density (a); thermodynamic pressure (b); Mach number (c); and magnetic pressure ($p_B = \mathbf{B} \cdot \mathbf{B}/2$) (d). It is clear from this demonstration problem that the method proposed is able to simulate and resolve torsional Alfvén waves, which are particularly visible in the plot of magnetic pressure, Figs. 6, 7, 8(d). The Mach number distribution (Figs. 6, 7, 8(c)) allows us to observe that

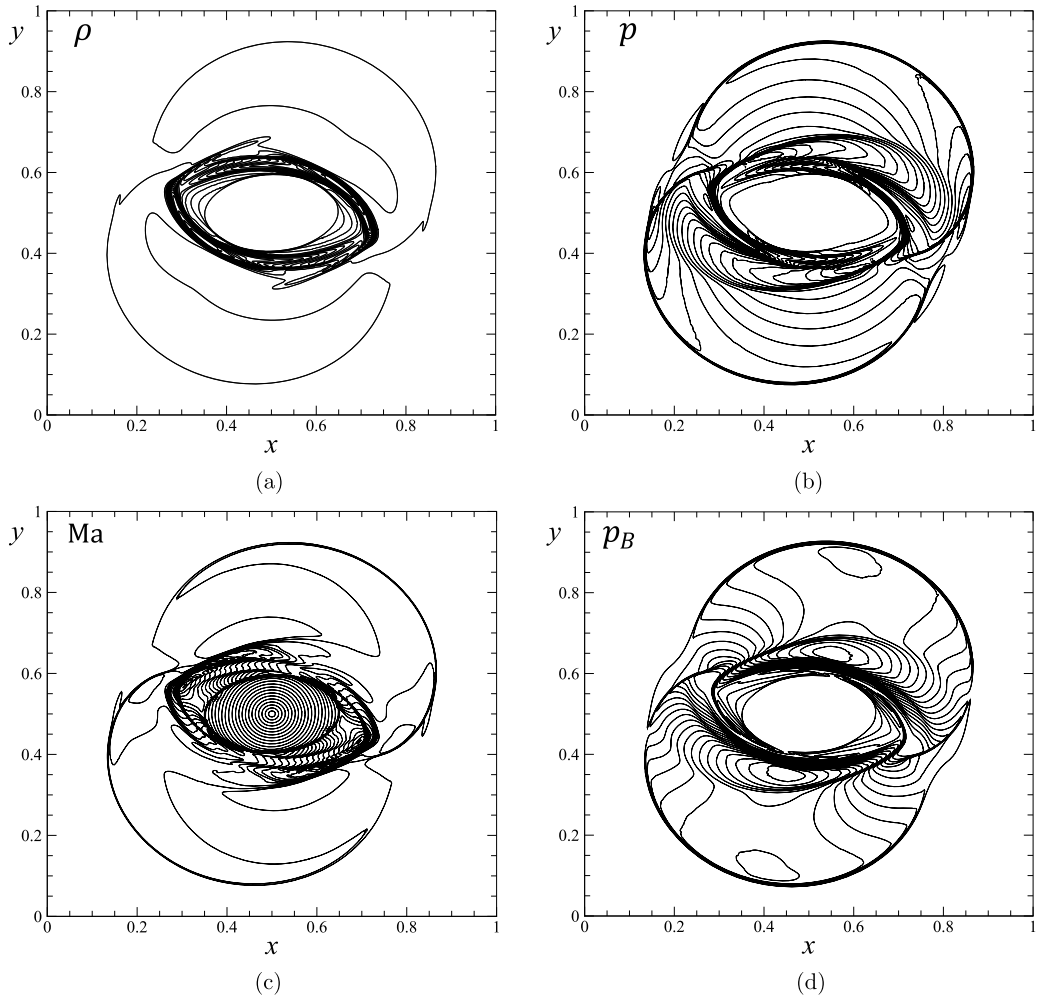


Fig. 8. Numerical results for the MHD rotor with the $N = 800$ grid at $t = 0.15$; contour plots of: density (a); thermodynamic pressure (b); Mach number (c); and magnetic pressure (d).

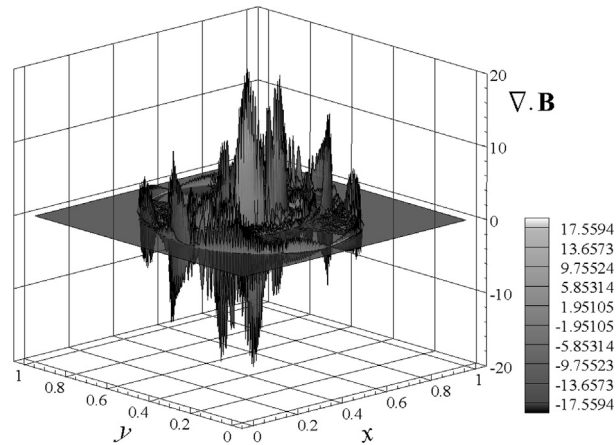


Fig. 9. Three-dimensional plot of $\nabla \cdot \mathbf{B}$ computed on the $N = 400$ grid. Notice that the numerical errors of significant magnitude appear only in the regions of discontinuity.

Table 1
Relative differences of pressure from the reference solution for the MHD cloud-shock and MHD rotor test cases.

Test-case	$N_x \times N_y$	h	δp_{ref}
Cloud-shock	50×50	0.02	0.00493
	100×100	0.01	0.00301
	200×200	0.005	0.00202
	400×400	0.0025	0.00038
Rotor	50×50	0.02	0.01070
	100×100	0.01	0.00611
	200×200	0.005	0.00237
	400×400	0.0025	0.00106

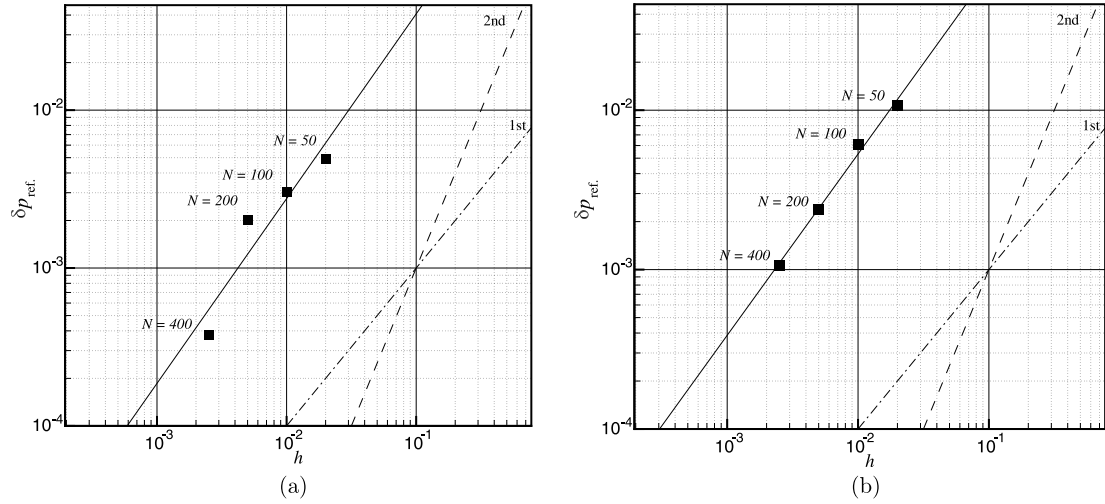


Fig. 10. Convergence plot for the pressure difference relatively to a reference solution, as a function of cell spacing h . Two test cases: (a) cloud-shock interaction; (b) MHD rotor.

the rotor is still rotating, up to a certain radial distance, with a uniform angular velocity. Beyond that distance the rotational speed decreases because the rotor exchanges angular momentum with the environment. All plots show a somewhat deformed cylinder as it is expected since the magnetic pressure will compress the cylinder on the upper and lower sides (along y), a phenomenon that is particularly visible in the density plot.

In Fig. 7(e) we present the magnetic field lines superimposed on the contour plot of pressure. It is clearly seen that, outside the region of influence of the Alfvén waves, the magnetic field basically maintains its initial value and direction, being oriented parallel to x -axis. However, inside the region of influence, the magnetic field is continuously refracted by each of the MHD discontinuities. A three-dimensional plot of the $\nabla \cdot \mathbf{B}$ computed on mesh $N = 400$ is presented in Fig. 9. As expected the numerical errors associated with the non-zero divergence of \mathbf{B} only appear with some expression in the regions of discontinuity.

To evaluate convergence with mesh refinement we have again computed the difference between the pressure field on any given mesh and on a reference mesh, as indicated by Eq. (56), and the relative errors are listed in Table 1 as a function of mesh spacing $h = 1/N$. The reference solution was computed on the finest mesh ($N = 800$) and the corresponding results are plotted in Fig. 10(b). The slope of this error measure decay falls again between the first- and second-order convergence slopes because, as the previous test case, the presence of strong MHD discontinuities switches off the second-order accuracy of the high-resolution TVD schemes.

4.2.3. MHD blast wave

The final ideal MHD problem considered for validation was the MHD blast wave, in which a circular pressure pulse (relative magnitude 10^4) expands outwards into a square region having a strong uniform magnetic field. This problem was introduced by Balsara [54] and was later retaken by the same author in a more thorough analysis [53,55]. It is a flow configuration known to cause positivity problems in several numerical hyperbolic methods if they are not developed with positivity-preserving properties. Negative pressures normally appear near the strong magnetosonic shock front, where there is a large discontinuity in pressure that could cause severe numerical problems when the plasma parameter $\beta = 2p/(\mathbf{B} \cdot \mathbf{B})$ is sufficiently small. We have solved this problem in a 200×200 uniform mesh with $x, y \in [0; 1]$ and we have specified the same initial conditions as Balsara [55] for all variables except the initial value of the magnetic field which we set to be half the value of [55], $B_x = B_y = 25/\sqrt{2}/\sqrt{4\pi}$. For this value of magnetic field the plasma β in the region outside the

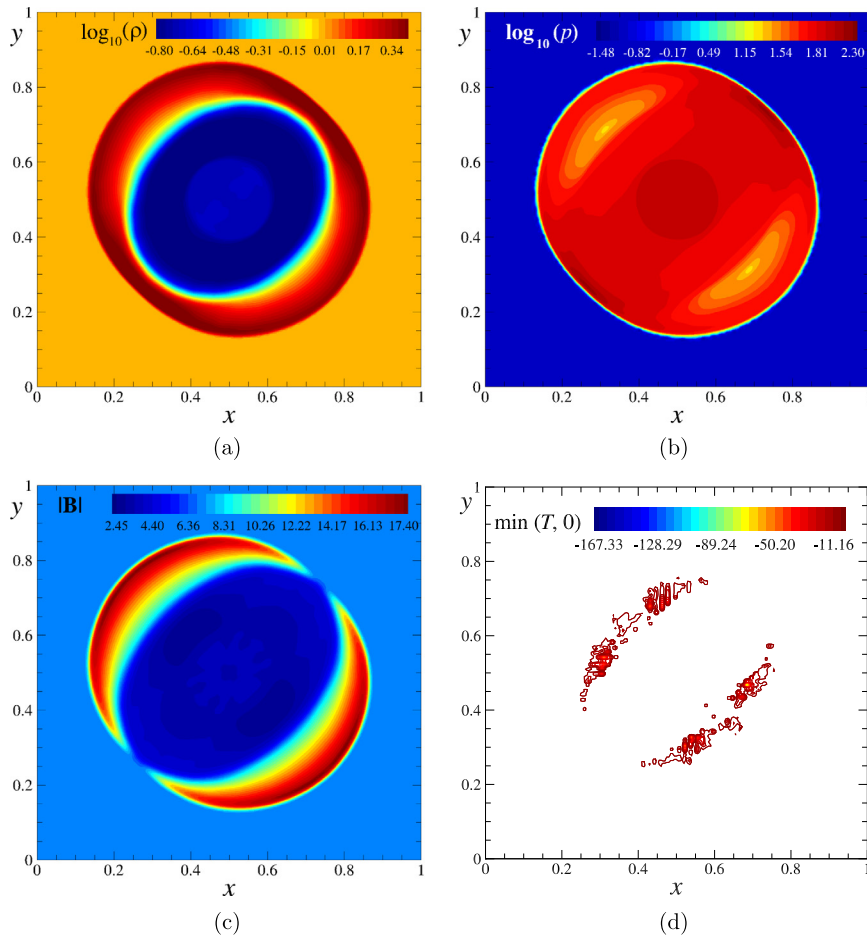


Fig. 11. MHD Blast wave: contour plot for density (a) and pressure (b) in a \log_{10} scale computed at $t = 0.012$. (c) Magnitude of the magnetic field for $t = 0.012$. (d) Contour plot showing the negative values of temperature for an initial $\beta = 0.001005$.

initial pressure pulse is equal to 0.004021, while in [55] it was 0.001005. We have reduced the value of \mathbf{B} by half because we found limitations in the numerical method at very low beta, with the appearance of negative temperatures as illustrated in Fig. 11(d), where negative values of T occur at $t = 0.007$ when the plasma β is set to 0.001005. These negative values appear in the shock front and, it should be remarked, were also observed with other numerical methods (see e.g. [56,57]). However, with our solution methodology this issue is more severe, leading to iterative converge problems, and for that reason we chose $\beta = 0.004021$ in this test case. Regarding the initial conditions for the other dependent variables, density assumes a value of unity over the whole domain, while pressure is equal to 0.1 outside a central circular region. This circular region is centered at $x, y = 0.5$ and has a radius of 0.1. Pressure inside this circle was set equal to 1000. The adiabatic ratio used for the calculation of other thermodynamic properties was $\gamma = 1.4$. In Figs. 11(a) and 11(b) we show the contour plots of density and pressure, respectively, in a logarithm scale, at the time instant $t = 0.012$. Fig. 11(c) shows the contour plot for the computed magnitude of the magnetic field. The main point to notice is that both density and pressure have positive values and, furthermore, the resolution of shocks seen in the figures is satisfactory.

5. Numerical modeling of a 2D MPD thruster

The MHD model we have tested and validated in the previous sections is now applied to compute a two-dimensional self-field MPD thruster. In particular, in this section we intend to study the effect of cathode size on the performance of such an MPD thruster. This type of analysis has been done both experimentally [58,59] and numerically, see e.g. [28,30,31, 46]. We will illustrate how some of the geometrical characteristics of the cathode have a strong influence on the discharge current pattern, which can result in an increase of the electro-thermal component of thrust.

Regarding the physical MHD model, equations of Section 2, several assumptions were made. The propellant gas is argon and we assumed that it is injected into the discharge chamber in a state of total ionization. It is then accepted that the plasma can be treated as a single, quasi-neutral fluid, in a state of thermal equilibrium ($T = T_e = T_i$, where the index e and i refers to electrons and ions, respectively). Several phenomena are also neglected, namely: viscous transport momentum;

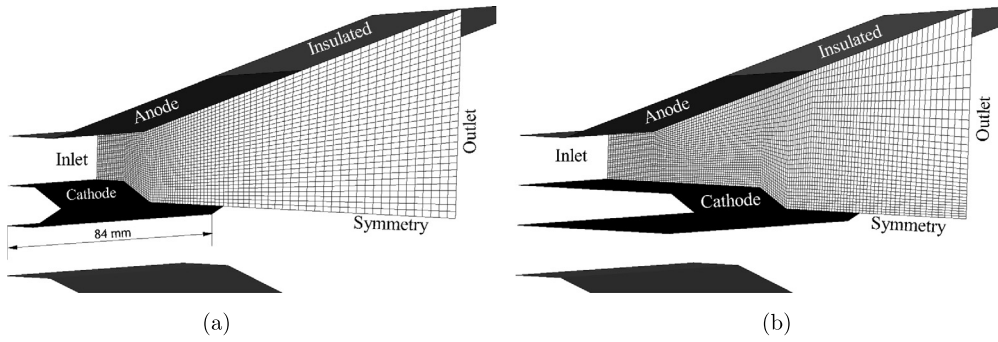


Fig. 12. Two-dimensional self-field MPD thruster geometry and boundary conditions: (a) Flared Anode Short Cathode (FASC); (b) Flared Anode Long Cathode (FALC).

heat conduction; electrical sheath; Hall effect; and radiation processes. Electrical resistivity is given by Spitzer–Härm formulation, see Eq. (9). The plasma flow is assumed to be purely bi-dimensional in the xy -plane, which means that the only non-vanishing component of the magnetic field will act in the z direction.

For the purpose of comparison with other studies we have used the same boundary conditions as Funaki et al. [28]. At inlet (Fig. 12), because the flow is in the subsonic regime, a mass flow rate of 2.5×10^{-3} kg/s is specified and a temperature of $T = 5000$ K is fixed. Since the flow is supersonic at outlet, all variables are extrapolated from the inside of the solution domain to the outlet plane. On the electrode walls a slip condition is imposed for the velocity field and a perfectly electrical conducting wall is specified for the magnetic field. For both the insulated wall and the symmetry plane the magnetic field is fixed to zero. At inlet the magnetic field is calculated as a function of the discharge current with the expression,

$$B_0 = \frac{\mu_0 I}{2W}, \quad (61)$$

where I is the discharge current and W represents the width of the thruster, in this case $W = 84 \times 10^{-3}$ m.

The two thruster configurations are presented in Fig. 12. Both geometries are composed by flared anodes (FA) and the only difference between the two devices is related to their cathode length. The first configuration, that we refer as FASC, is composed by a short cathode with a length equal to 13×10^{-3} m, while the second geometry (FALC) is composed by a long cathode with 40×10^{-3} m of length.

In Figs. 13(a), 13(c) we present the computed contour plots for the magnitude of velocity, for an imposed discharge current of $I = 8000$ A. The FASC configuration is able to achieve a higher exhaust velocity (12000 m/s against 7000 m/s). The same trend was observed experimentally by Funaki et al. [26] and numerically by different authors [28,30,46]. The electrical current distribution, obtained for a discharge current of $I = 2500$ A, is plotted in Figs. 13(b), 13(d). We can see that, due to the cathode geometrical shape, the current lines have a tendency to accumulate near the cathode tip and that the concentration is more noticeable in the short cathode configuration. Such concentration of current near the tip of the short cathode will generate an increase of the Joule heating effect, which will consequently increase the electro-thermal component of thrust, and thus resulting in higher exhaust velocity.

We compare now our method against experimental [26] and numerical results from different authors [28,30]. In Fig. 14(a) results for the axial velocity distribution along the section $y = 0.009$ m, for the FASC configuration, are compared with the solution obtained by two groups of authors. This section is shown in Fig. 13 (indicated as section a-a) and the velocity profile was calculated for an inlet discharge current of $I = 8000$ A. This comparison illustrates that our computed velocity is only slightly lower at the thruster outlet but the trend of the axial velocity variation is well captured by the present predictions. A more realistic validation would require a comparison against experimental data. For that purpose, in Fig. 14(b), the numerical results obtained for the momentum thrust in the FASC configuration are compared with the experimental ones of Ref. [26]. It is seen that the present MHD model over-predicts the measured propulsion force. Nevertheless, the trend is the same and when our predicted solution is compared with numerical results obtained by others authors [30], who have employed a similar numerical model, we observe a much better match and the curves follow each other very well.

We turn now our attention to several of the thruster parameters defined in Section 3.4 in order to ascertain the possible effects of cathode length on the plasma flow. In Fig. 15(a) we compare the predicted thrust values for the two cathode configurations, as a function of discharge current. We see that the short cathode configuration allows us to reach higher values of thrust, which is advantageous.

In order to understand the discrepancy between the overall thrust for the two devices it is useful to decompose the total force in their electromagnetic (F_{ELM}) and thermal components (F_{Therm}) (Eqs. (50)–(51)). Fig. 15(b) shows that the ELM component of thrust is almost the same for both cathode lengths, but a significant discrepancy appears in the thermal component of thrust. We have already pointed out that this instance is related to the geometrical shape of the cathode, which allows a larger concentration of discharge current lines around its tip, and therefore tends to an increase of the electro-thermal component of thrust. Fig. 15(b) also reveals that in the computed range of discharge current, the thermal

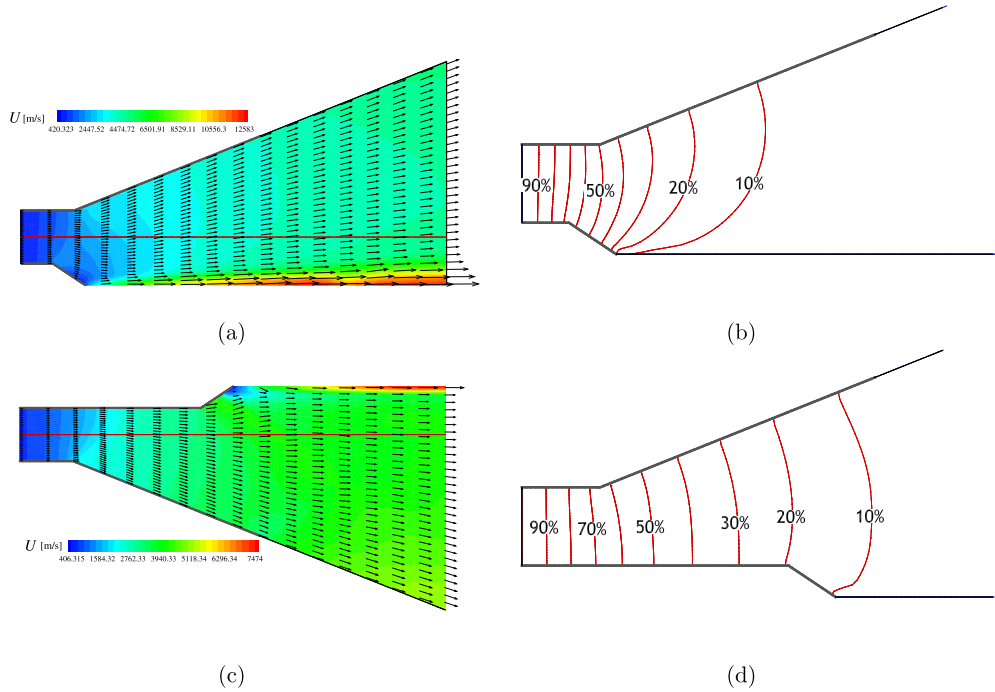


Fig. 13. Contour plots for the velocity magnitude superimposed on the corresponding vectors, for the FASC (a) and the FALC (c) configurations. The plots (b) and (d) show the electric current distribution as a percentage of the inlet value.

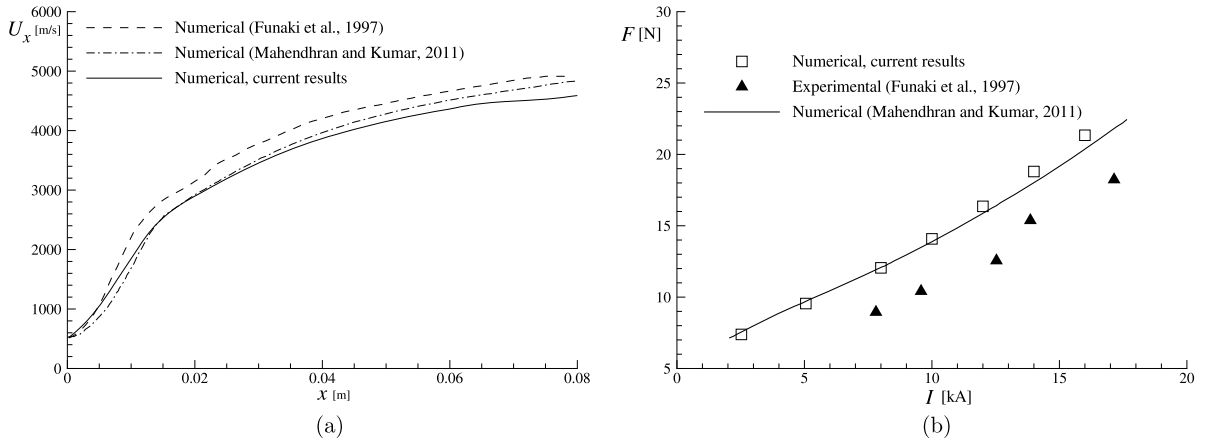


Fig. 14. Comparison between experimental and numerical results. (a) Axial velocity profile along the $y = 9$ mm line. (b) Momentum thrust as a function of inlet discharge current.

component of thrust is superior to the electromagnetic component until a discharge current of $I \approx 13$ kA is reached for the FASC configuration, or a discharge current of $I \approx 12$ kA for the FALC device, Eqs. (50)–(51).

The results for thruster efficiency and specific impulse are presented in Fig. 16. The FASC configuration can achieve the highest efficiency for the computed range of discharge currents. This could be expected since, for the same mass flow rate and discharge current, that configuration results in higher values of thrust.

6. Conclusions

In this paper a numerical method for resistive and viscous MHD flow is explained and applied to a number of demonstration test problems. This method is here validated for viscous and resistive MHD flows in particular by using the analytical solutions valid for the Shercliff and Hunt flow test cases. It was also validated for complex shock wave interaction using three standard two-dimensional ideal MHD problems. From the results obtained with the various test cases here considered we reach the conclusion that our method is able to handle a large variety of MHD flows, ranging from the near incompress-

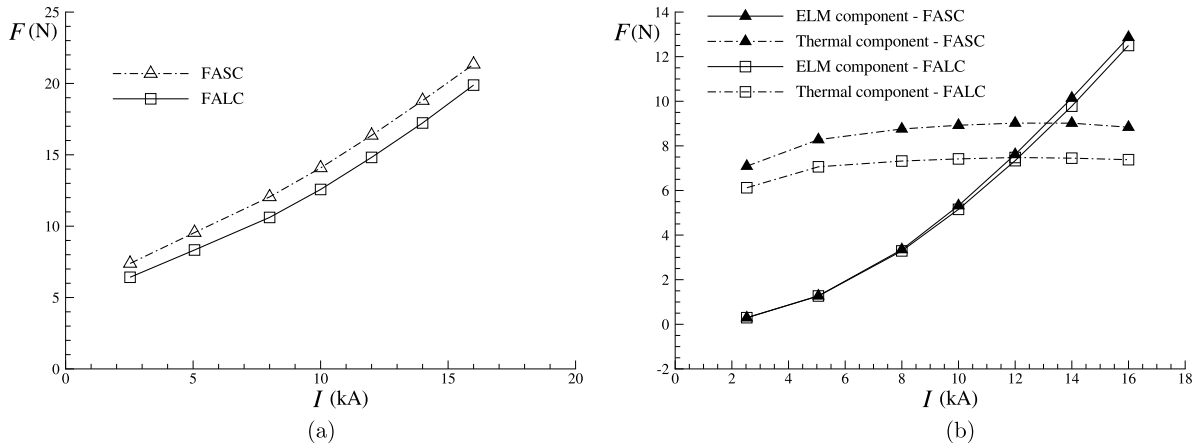


Fig. 15. MPD numerical results for thrust with the FASC and FALC configurations (a). The thermal component of thrust (b) is the main responsible for the discrepancy between FASC and FALC configurations.

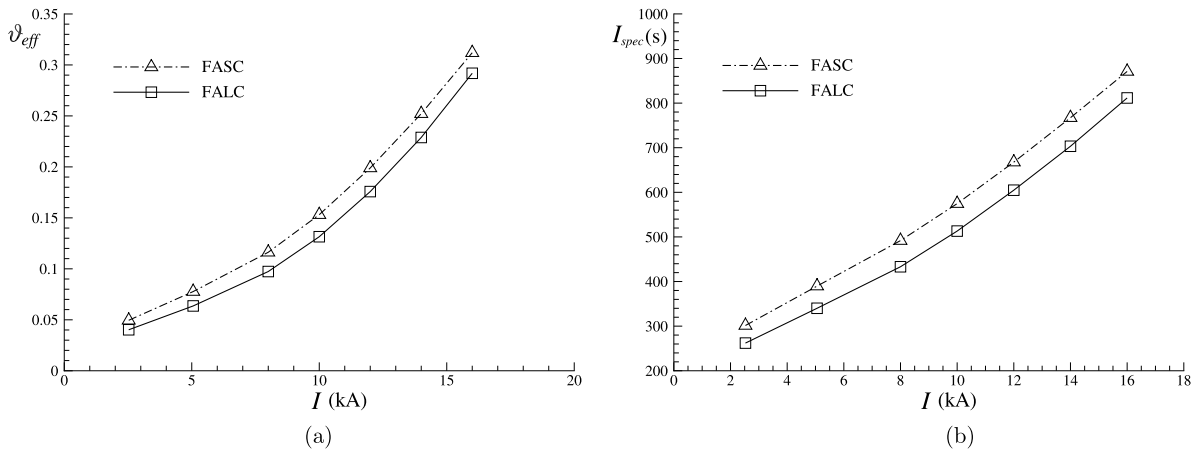


Fig. 16. MPD thruster results for efficiency (a) and specific impulse (b). As expected, the FASC configurations give higher specific impulse and efficiency.

ible to highly compressible regimes. However, the last test case here considered revealed a limitation when the method is applied to the computation of very low- β flows. We found that, for values lower than $\beta = 0.004$, the MHD blast wave test-case results in numerical instabilities due to the absence of a positivity-preserving technique in our methodology. In order to properly address this issue, future developments may include a self-adjusting positivity preserving technique similar to that suggested by Balsara [55].

An application case is also addressed, the modeling of a two-dimensional self-field MPD nozzle. A comparison between the computed values for the momentum thrust and experiments shows at first instance, that the current model over-predicts the thrust. However, assumptions of total ionization and thermal equilibrium may lead to an over-prediction of temperature, thus resulting in a larger thermal component of thrust. One way of improving the results can be attained with the addition of ionization models, multi-specie energy equations and real gas theory.

The effect of MPD electrode geometrical parameters on the thruster performance was also analyzed. We have demonstrated that by enhancing the electro-thermal component of thrust, higher overall thrust values will result. In a self-field MPD thruster this can be achieved by reducing the cathode length.

References

- [1] K. Sankaran, L. Martinelli, S.C. Jardin, E.Y. Choueiri, *Int. J. Numer. Methods Eng.* 53 (2002) 1415–1432.
- [2] M. Brio, C. Wu, *J. Comput. Phys.* 75 (1988) 400–422.
- [3] A.L. Zachary, A. Malagoli, P. Colella, *SIAM J. Sci. Comput.* 15 (1994) 263–284.
- [4] D. Ryu, T.W. Jones, *Astron. Astrophys.* 442 (1995) 228–258.
- [5] P. Roe, D. Balsara, *SIAM J. Appl. Math.* 56 (1996) 57–67.
- [6] P. Cargo, G. Gallice, *J. Comput. Phys.* 136 (1997) 446–466.
- [7] K.G. Powell, P.L. Roe, T.J. Linde, T.I. Gombosi, D.L.D. Zeeuw, *J. Comput. Phys.* 154 (1999) 284–309.
- [8] G. Tóth, D. Odstrčil, *J. Comput. Phys.* 128 (1996) 82–100.
- [9] T. Linde, *Int. J. Numer. Methods Fluids* 40 (2002) 391–402.

- [10] S. Li, J. Comput. Phys. 203 (2005) 344–357.
- [11] T. Miyoshi, K. Kusano, J. Comput. Phys. 208 (2005) 315–344.
- [12] S. Han, J. Lee, K. Kim, AIAA J. 47 (2009) 970–981.
- [13] D.S. Balsara, J. Comput. Phys. 229 (2010) 1970–1993.
- [14] D.S. Balsara, J. Comput. Phys. 231 (2012) 7476–7503.
- [15] D.S. Balsara, M. Dumbser, R. Abgrall, J. Comput. Phys. 261 (2014) 172–208.
- [16] D.S. Balsara, J. Comput. Phys. 174 (2001) 614–648.
- [17] R. Keppens, Z. Meliani, A. van Marle, P. Delmont, A. Vlasis, B. van der Holst, in: Computational Plasma Physics Special Issue: Computational Plasma Physics, J. Comput. Phys. 231 (2012) 718–744.
- [18] J. Rincón, R. Elder, Comput. Fluids 26 (1997) 217–231.
- [19] D.R. van der Heul, C. Vuik, P. Wesseling, Comput. Fluids 32 (2003) 1113–1132.
- [20] J.C. Henriques, L.M. Gato, Comput. Fluids 33 (2004) 755–769.
- [21] C.M. Xisto, J.C. Páscoa, P.J. Oliveira, D.A. Nicolini, Int. J. Numer. Methods Fluids 70 (8) (2012) 961–976.
- [22] D.R. van der Heul, C. Vuik, P. Wesseling, Int. J. Numer. Methods Fluids 40 (2002) 521–529.
- [23] C.M. Xisto, J.C. Páscoa, P.J. Oliveira, Int. J. Numer. Methods Fluids 72 (11) (2013) 1165–1182.
- [24] M.R. LaPointe, P.G. Mikellides, in: 37th Joint Propulsion Conference and Exhibit, 2011, AIAA-2001-3499.
- [25] K. Toki, M. Sumida, K. Kuriki, J. Propuls. Power 8 (1992) 93–97.
- [26] I. Funaki, K. Toki, K. Kuriki, J. Propuls. Power 14 (1998) 1043–1048.
- [27] P. Sleziona, M. Auweter-Kurtz, H. Schrade, in: Proc. 20th International Electric Propulsion Physics Conference, Garmisch-Partenkirchen, 1988, IEPS-88-043.
- [28] I. Funaki, K. Toki, K. Kuriki, J. Propuls. Power 13 (1997) 789–795.
- [29] R.M. Myers, M.A. Mantieneks, M.R. Lapointe, MPD thruster technology, Technical Report NASA-TM-105242, NASA Glenn Research Center, 1991.
- [30] M. Mahendhran, A. Kumar, in: 32nd International Electric Propulsion Conference, Wiesbaden, Germany, 2011, IEPC-2011-228.
- [31] M.R. LaPointe, Numerical simulation of geometric scale effects in cylindrical self-field MPD thrusters, Technical Report CR-189224, NASA Lewis Research Centre, 1992.
- [32] P.C. Sleziona, M. Auweter-Kurtz, H.O. Schrade, in: Proceedings of 23rd International Electric Propulsion Conference, Seattle, 1993, IEPC-93-066.
- [33] T. Miyasaka, T. Fujiwara, in: Joint Propulsion Conferences, American Institute of Aeronautics and Astronautics, 1999.
- [34] A. Dedner, F. Kemm, D. Kröner, C.-D. Munz, T. Schnitzer, M. Wesenberg, J. Comput. Phys. 175 (2002) 645–673.
- [35] D.S. Balsara, J. Kim, Astrophys. J. 602 (2004) 1079–1090.
- [36] P. Mocz, M. Vogelsberger, L. Hernquist, Mon. Not. R. Astron. Soc. 442 (1) (2014) 43–55.
- [37] M.R. Lapointe, in: Joint Propulsion Conference, Sacramento, 1991, AIAA-91-2341.
- [38] R.I. Issa, J. Comput. Phys. 62 (1986) 40–65.
- [39] R.I. Issa, M.H. Javareshkian, AIAA J. 36 (1998) 1652–1657.
- [40] K.H. Kim, J.H. Lee, O.H. Rho, Comput. Fluids 27 (1998) 311–346.
- [41] C.D. Meyer, D.S. Balsara, T.D. Aslam, Mon. Not. R. Astron. Soc. 422 (2012) 2102–2115.
- [42] C.D. Meyer, D.S. Balsara, T.D. Aslam, J. Comput. Phys. 257 (2014) 594–626, Part A.
- [43] M.S. Liou, J. Comput. Phys. 214 (2006) 137–170.
- [44] M.A. Alves, P.J. Oliveira, F.T. Pinho, Int. J. Numer. Methods Fluids 41 (2003) 47–75.
- [45] K. Kubota, I. Funaki, Y. Okuno, IEEE Trans. Plasma Sci. 37 (2009) 2390–2398.
- [46] K. Kubota, I. Funaki, Y. Okuno, in: 30th International Electric Propulsion Conference, Florence, Italy, 2007, IEPC-07-87.
- [47] J.A. Shercliff, Math. Proc. Camb. Philos. Soc. 49 (1953) 136–144.
- [48] J.C.R. Hunt, J. Fluid Mech. 21 (1965) 577–590.
- [49] M.-J. Ni, R. Munipalli, P. Huang, N.B. Morley, M.A. Abdou, J. Comput. Phys. 227 (2007) 205–228.
- [50] J. Priede, S. Aleksandrova, S. Molokov, J. Fluid Mech. 649 (2010) 115–134.
- [51] W. Dai, P.R. Woodward, J. Comput. Phys. 142 (1998) 331–369.
- [52] G. Tóth, J. Comput. Phys. 161 (2000) 605–652.
- [53] D.S. Balsara, D.S. Spicer, J. Comput. Phys. 149 (1999) 270–292.
- [54] D.S. Balsara, Astrophys. J. Suppl. Ser. 116 (1998) 133–153.
- [55] D.S. Balsara, J. Comput. Phys. 231 (2012) 7504–7517.
- [56] S. Li, J. Comput. Phys. 227 (2008) 7368–7393.
- [57] F. Li, L. Xu, J. Comput. Phys. 231 (2012) 2655–2675.
- [58] I. Funaki, K. Kuriki, K. Toki, J. Propuls. Power 14 (1998) 1043–1048.
- [59] D. Nakata, K. Toki, I. Funaki, Y. Shimizu, H. Kuninaka, Y. Arakawa, in: 29th International Electric Propulsion Conference, 2005, IEPC-05-163.